

[Skip to main content](#)[Skip to article](#)

Brought to you by: [Colorado School of Mines](#)

- [Journals & Books](#)
- [Help](#)
- [Search](#)
- [My account](#)

Colorado School of Mines

- [View PDF](#)
- Download full issue

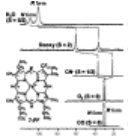
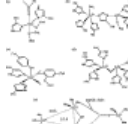
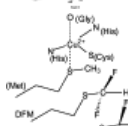



## Outline

1. [Abstract](#)
2. [Keywords](#)
3. [1. Introduction](#)
4. [2. Methods](#)
5. [3. Applications to metalloproteins](#)
6. [4. Applications to paramagnetic metal complexes of biological interest](#)
7. [5. Conclusion](#)
8. [Acknowledgement](#)
9. [References](#)

Show full outline

## [Cited by \(18\)](#)

## Figures (15)

1. 
  2. 
  3. 
  4. 
  5. 
  6. 
- Show 9 more figures

## Tables (2)

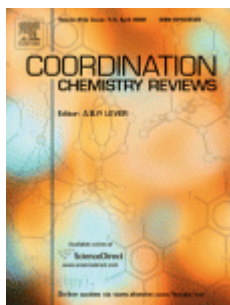
1. [Table 1](#)
2. [Table 2](#)



ELSEVIER

## [Coordination Chemistry Reviews](#)

[Volume 253, Issues 7–8](#), April 2009, Pages 963–976



### Review

## **$^{19}\text{F}$ NMR: An underused efficient probe for paramagnetic metal centers in bioinorganic solution chemistry**

Dedicated to Professor Jan Reedijk on the occasion of his 65th birthday.

Author links open overlay panelCatherine Belle, Claude Béguin, Sylvain Hamman, Jean-Louis Pierre

Show more

Add to Mendeley

Share

Cite

<https://doi.org/10.1016/j.ccr.2008.06.015>[Get rights and content](#)

### Abstract

The application of solution studies in bioinorganic chemistry through paramagnetic  $^{19}\text{F}$  NMR is briefly reviewed. In Section 2 we summarize some theoretical aspects. Selected applications from bioinorganic chemistry (enzymes and models) can be found in Sections 3 and 4.

- [Previous article in issue](#)
- [Next article in issue](#)

### Keywords

Metalloproteins

Biomimetic model complexes

$^{19}\text{F}$  NMR

Paramagnetic metal centers

### 1. Introduction

As paramagnetic metal centers play a paramount role in the chemistry of metalloproteins and their biomimetic models, as well as simple transition metal complexes, specific tools for solution studies of their structure and their catalytic activities are requested.

Among the various spectroscopies used for these purposes,  $^{19}\text{F}$  NMR seems to have been underused despite its great potentiality. The utility of  $^{19}\text{F}$  NMR spectroscopy in biological molecules studies, in particular to probe protein structure has previously been demonstrated and was reviewed several years ago [1], [2], [3]. Fluorine NMR has also been applied to the study of biochemical mechanisms, metabolism, biodistribution, screening and pharmacokinetics of several fluorinated drugs.

In this manuscript the broad range of potential applicability of paramagnetic  $^{19}\text{F}$  NMR in bioinorganic chemistry field (proteins and models) is reviewed with emphasis on selected examples, most of them from our work. Our goal is to bring forward an underused tool and impulse future utilization.

## 2. Methods

### 2.1. $^{19}\text{F}$ NMR: a brief reminder

$^{19}\text{F}$  is a 100% naturally abundant nucleus with a nuclear spin  $I = 1/2$ .  $^{19}\text{F}$  has a high-magnetogyric ratio  $\gamma$ , about 0.94 times that of  $^1\text{H}$  (the reduced magnetogyric ratio  $\gamma_F$  value is  $40.054 \text{ MHz T}^{-1}$ ). Therefore, its sensitivity, at constant field for equal number of nuclei, is 0.83 as compared to  $^1\text{H}$  so that fluorine-containing compounds produce NMR signals that are nearly as easily detected as those of  $^1\text{H}$ . For diamagnetic molecules, the range of chemical shifts for  $^{19}\text{F}$  compounds is 20 or more times that of  $^1\text{H}$ . For instance, the substituent effect in *para* substituted fluorobenzenes is about 20 ppm with the usual substituents (from *p*- $\text{NO}_2$  to *p*- $\text{OCH}_3$ ). This large effect provides a better resolution of signals and also a larger dynamic range giving an ability to differentiate between signals arising from species, which are in a dynamic equilibrium.  $^{19}\text{F}$  chemical shifts are officially (IUPAC) reported with reference to external  $\text{CFCl}_3$  [4]. Secondary references are ordinarily used as external  $\text{C}_6\text{F}_6$  according to  $\delta_F(\text{C}_6\text{F}_6) = -163 \text{ ppm}$  relative to  $\text{CFCl}_3$  or as external  $\text{CF}_3\text{COOH}$  according to  $\delta_F(\text{CF}_3\text{COOH}) = -79 \text{ ppm}$  relative to  $\text{CFCl}_3$ . With the nuclear spin quantum  $1/2$ , the relaxation is usually sufficiently long so that spin–spin splitting may be resolved easily.

Fluorine is particularly useful as a tracer in biological systems since there is essentially no natural background and the  $^{19}\text{F}$  NMR signals are only related to the few  $^{19}\text{F}$  nuclei in the ligand or in the protein. This labeling is particularly valuable from two points of view: (i) the Van der Waals radius of a fluorine atom is only slightly larger than that of an hydrogen atom, *i.e.* 135 and 110 pm for fluorine and hydrogen, respectively; (ii) at least when one fluorine is introduced in aromatic structures, there is a compensation of electronic effects giving only a small perturbation in the electronic structure of the molecule. Introduction of a strongly electron-withdrawing  $\text{CF}_3$  or  $\text{C}_6\text{F}_5$  group can induce marked effects on the physicochemical properties of the considered compound, however care should be taken regarding perturbations in the electronic structure of the molecule.

### 2.2. $^{19}\text{F}$ NMR and paramagnetism

The fluorine nucleus in paramagnetic metal systems as in molecular complexes or in metalloproteins is sensitive to the paramagnetic effect through the relaxation and the chemical shift parameters [5], [6], [7]. The effects can be considerable on relaxation, on chemical shift parameters or on both.

#### 2.2.1. Electron-induced nuclear relaxation

The nuclear spin relaxation in a paramagnetic complex is induced by the electron–nucleus hyperfine interaction between the  $^{19}\text{F}$  nucleus spin  $I$  and the electron spin  $S$ . This effect is characterized by the relaxation rate  $R_M$  ( $1/T_M$  where  $T_M$  is the relaxation time) with  $i = 1$  or  $2$  according to the spin–lattice or spin–spin mechanism of relaxation, respectively. The general effect is an enhancement and is commonly called paramagnetic relaxation enhancement (PRE). The set of equations for the relaxation rates in these systems are known [8], [9], [10], [11], [12], [13] as the Solomon–Bloembergen–Morgan (SBM) Eqs. [8], [9]. These equations necessitate some comments before their detailed explanation.

The electron–nuclear hyperfine interaction between the nuclear spin (here the  $^{19}\text{F}$  nucleus) and the electron spin consists mainly of two contributions:

(i)

The first term, the dipole–dipole (DD or dipolar) contribution or pseudo-contact coupling, results from the through-space dipolar interaction between the nuclear spin  $I$  and the electronic spin  $S$ . The derivation comes from the dipolar interaction Hamiltonian with the dipole–dipole coupling constant  $C_{DD}$  (in  $\text{rad s}^{-1}$ ):  $C_{DD} = \mu_0 4\pi \gamma_I \gamma_S / r_{IS}^3$  with  $\gamma_S = -g_S \mu_B$  and the other symbols having their usual meaning. This formula shows the decay of this constant with  $r_{IS}^{-3}$  (where  $r_{IS}$  is the electron–nucleus distance). The treatment needs the spectral density function of the intramolecular dipolar interaction. For an isotropic Brownian rotation of the complex, the corresponding auto-correlation function is monoexponential with one rotational correlation time  $\tau_R$ , and its Fourier transform is a Lorentzian spectral density function depending on the angular frequency  $\omega$  as  $J(\omega, \tau_R) = \tau_R / (1 + \omega^2 \tau_R^2)$

The standard relaxation theory gives the following expressions for the longitudinal  $R_{1DD}$  and transversal  $R_{2DD}$  relaxation rate:  $R_{1DD} = 215 C_{DD}^2 S(S+1) [J(\omega_S - \omega_I) + 3J(\omega_I) + 6J(\omega_S + \omega_I)]$  (4)  $R_{2DD} = 115 C_{DD}^2 S(S+1) [4J(0) + 3J(\omega_I) + J(\omega_S - \omega_I) + 6J(\omega_S) + 6J(\omega_S + \omega_I)]$

As  $\omega_I$  is much smaller than  $\omega_S$ , the reduced formula gives  $R_{1DD} \approx 215 C_{DD}^2 S(S+1) [3J(\omega_I) + 7J(\omega_S)]$  (5)  $R_{2DD} \approx 115 C_{DD}^2 S(S+1) [4J(0) + 3J(\omega_I) + 13J(\omega_S)]$  (6)

The appropriate correlation times in the expression of the spectral density function are related to the fluctuations rate of the electron spin dipolar field caused by three main random motions:

(1)

The overall rotation of the complex characterized by the correlation time  $\tau_R$  of the complex.

(2)

The chemical exchange rate of the metal bound ligand in dynamic equilibrium with the free ligand in the solution, characterized by the coordination lifetime  $\tau_M$ . In most cases, we have  $\tau_M \ll \tau_R$  and both are larger than the electronic relaxation time. Otherwise, the time correlation between the values of the interspin vector  $r \rightarrow IS$  when the ligand changes from its bound to free states should be taken into account and the theory becomes significantly more complicated [14].

(3)

The rate of the statistical changes of the quantum states of the electronic spin characterized by the electronic relaxation rates of the  $R_S$  of the complexed metal. The terms at frequencies  $0$  and  $\omega_I$  correspond to the part of the dipolar Hamiltonian involving the component  $S_z$  of  $S$ , whereas the terms at frequencies  $\omega_S - \omega_I$ , and  $\omega_S + \omega_I$ , or simply  $\omega_S$ , stem from the components  $S_+$  or  $S_-$  of this Hamiltonian. The component  $S_z$  gives rise to the longitudinal relaxation rate  $R_{1S}$  and the components  $S_+$  or  $S_-$  are at the origin of the transversal relaxation rate  $R_{2S}$ .

Therefore, the appropriate correlation times for the dipolar interaction are  $\tau_{ci} = \tau_R^{-1} + \tau_M^{-1} + R_i S \approx \tau_R^{-1} + R_i S$

When one of these times is much shorter than the others, it effectively dominates  $\tau_c$ . With some metal ions,  $R_S$  dominates; but it is not the case for the metal ions considered in this review ( $\text{Cu}^{\text{II}}$ ,  $\text{Fe}^{\text{III}}$ ,  $\text{Mn}^{\text{II}}$ ,  $\text{Gd}^{\text{III}}$ , ...).

Finally, the formulas generally used to calculate the paramagnetic relaxation enhancements due to the electron–nuclear dipole–dipole coupling are (8)  $R_{1\text{DD}} = 215CDD2S(S+1)3\tau_c11 + \omega l2\tau_c12 + 7\tau_c21 + \omega S2\tau_c22$  (9)  $R_{2\text{DD}} = 115CDD2S(S+1)4\tau_c1 + 3\tau_c11 + \omega l2\tau_c12 + 13\tau_c21 + \omega S2\tau_c22$

Recently, the theory of the PRE of nuclear spins as a function of magnetic field was thoroughly revisited [15], [16]. For the low-field cases ( $\omega_l \ll$  the zero field splitting in the complex), the previous formulas should be unfortunately replaced by non-analytical equations. For the high-field cases ( $\omega_l \gg$  ZFS), the last term of each formula have to be dropped and the high-field PRE can be approximated by the analytical expressions: (10)  $R_{1\text{DDhighfield}} = 25CDD2S(S+1)\tau_c11 + \omega l2\tau_c12$  (11)  $R_{2\text{DDhighfield}} = 115CDD2S(S+1)4\tau_c1 + 3\tau_c11 + \omega l2\tau_c12$

(ii)

The second term is the through-bonds scalar coupling (SC) or Fermi contact coupling or hyperfine contribution. It arises from bond interactions between the fluorine nuclear spin and the spin of electron density at the site of observed nucleus. Its value is directly proportional to the local spin density in s-type atomic orbitals and allows derivation of the corresponding hyperfine coupling constant. This contact term is unaffected by the reorientation of the complex  $\tau_R$ .

Starting from the Fermi contact interaction  $AIS$ , where  $I$  and  $S$  are the dimensionless spin operators for the fluorine nucleus and the paramagnetic electrons and  $A$  is the coupling constant (in  $\text{rad s}^{-1}$ ), and introducing the appropriate spectral density function  $J_\omega$ , the Fermi contact contributions to the relaxation rates are [7], [9], [13] (12)  $R_{1\text{SC}} = 23A^2S(S+1)J(\omega S - \omega_l) = 23A^2S(S+1)J(\omega S)$  (13)  $R_{2\text{SC}} = 13A^2S(S+1)[J(0) + J(\omega S - \omega_l)] \approx 13A^2S(S+1)[J(0) + J(\omega S)]$

The final standard Fermi contact formulas are (14)  $R_{1\text{SC}} = 23A^2S(S+1)\tau'^c_{21} + \omega S2\tau'^c_{22}$  (15)  $R_{2\text{SC}} = 13A^2S(S+1)\tau'^c_{11} + \tau'^c_{21} + \omega S2\tau'^c_{22}$  where  $\tau'^c_{ci}$  is the appropriate correlation time for the Fermi contact relaxation. It differs from the previous  $\tau_c$  correlation time for the dipole–dipole interaction, as the overall reorientation of the complex in solution has no effect on the contact term, i.e. (16)  $\tau'^c_{ci} = \tau_M - 1 + R_iS$

Again, the simple Eqs. (14), (15) have to be replaced by non-analytical equations at low field [15], [16], whereas at high field, the contribution in  $\omega_S$  has to be dropped.

(iii)

In deriving the dipolar and contact relaxation contributions due to the presence of unpaired electrons, the small difference in the population of the electron spin levels according to the Boltzmann distribution has been neglected. When this effect is taking into account, a time-averaged magnetic moment of the complex occurs and its interaction with the nuclear spins provides a further relaxation contribution, called magnetic susceptibility relaxation or Curie spin relaxation [7]. The corresponding correlation time is only determined by  $\tau_R$  and  $\tau_M$  according to (17)  $\tau'^c_{ci} = \tau_R - 1 + \tau_M - 1 \approx \tau_R - 1$

The dipolar contributions to the relaxation rates provided by this mechanism

are (18)  $R_{1\text{DDCurie}} = 25CDD2BogS\mu BS(S+1)3kT23\tau'^c_{11} + \omega l2\tau'^c_{22}$  (19)  $R_{2\text{DDCurie}} = 15CDD2BogS\mu BS(S+1)3kT2(4\tau'^c_{11} + 3\tau'^c_{21} + \omega l2\tau'^c_{22})$

(iv)

As  $^{19}\text{F}$  nucleus is sensitive to the chemical shift anisotropy, the CSA mechanism could be present [7], [17]. As most of the studies are made at frequencies less than 500 MHz, this CSA effect is always shown to be negligible in comparison with the PRE.

## 2.2.2. Electron-induced paramagnetic chemical shift

The paramagnetic chemical shift (called also hyperfine shift or paramagnetic isotropic shift)  $\Delta\delta_M$  can be defined as the difference  $\Delta\delta_M = \delta_{\text{obs}} - \delta_D$ , where  $\delta_{\text{obs}}$  is the shift observed in the paramagnetic solution and  $\delta_D$  is the diamagnetic chemical shift, which would be observed if the paramagnetic ion was replaced by a diamagnetic analog (e.g.  $\text{Eu}^{\text{III}}/\text{Lu}^{\text{III}}$  or  $\text{Cu}^{\text{II}}/\text{Zn}^{\text{II}}$ ). This paramagnetic shift has two components, the pseudo-contact (or dipolar) contribution  $\Delta\delta\text{MDD}$  and the contact (or Fermi) contribution  $\Delta\delta\text{MSC}$ :

(i)

The pseudo-contact contribution originates from the anisotropy of the paramagnetic susceptibility tensor of the complex. In the metal-centered point-dipole approximation, evaluation of the effect can be done, using the Cartesian components of the susceptibility tensor with the Cartesian axes chosen along the principal directions of this tensor, the classical expression for  $\Delta\delta\text{MDD}$  is [7],

[18] (20)  $\Delta\delta\text{MDD} = D1(1 - 3\cos2\theta) + D2\sin2\theta\cos2\phi$  (21) with  $D1 = 112\pi r l S3\chi_{zz} - 12(\chi_{xx} + \chi_{yy})$  and  $D2 = 18\pi r l S3(\chi_{xx} - \chi_{yy})$ , respectively and  $r_{lS}$ ,  $\theta$  and  $\phi$  are the polar coordinates of the interspin vector  $r \rightarrow IS$  joining the nucleus under examination and the electronic spin in the principal axes system of the susceptibility tensor.

In the case of axial symmetry of the complex ( $\chi_{xx} = \chi_{yy}$ ), the equation reduces to (22)  $\Delta\delta\text{MDD} = D3\cos2\theta - 1r3$  giving a zero pseudo-contact shift for  $\theta = 54^\circ 44'$ .

For a complex with only one thermally populated multiplet with spin  $S$ , the susceptibility terms  $\chi_{ii}$  are related to the corresponding component  $g_{ii}$  of the tensor  $\mathbf{g}$  according the following formula: (23)  $\chi_{ii} = N\mu_B2S(S+1)3kBTg_{ii}2$

The  $\Delta\delta\text{MDD}$  paramagnetic shift is therefore varying as  $T^{-1}$ .

In the presence of crystal field or zero-field splitting (ZFS) effects, the susceptibility tensor can be calculated through the Van Vleck equation [7], [18]. In general, these effects lead to an additional contribution in  $T^{-2}$  to  $\Delta\delta\text{MDD}$  [7], [19]. For ions of the first transition series, it can be shown that for axial symmetry with not too high values of  $|g_{\parallel}^2 - g_{\perp}^2|$ , the term in  $T^{-1}$  is small, but the term in  $T^{-2}$  is sizable [7], [20]. For paramagnetic  $\text{Ln}^{\text{III}}$  ions, but  $\text{Gd}^{\text{III}}$ , the term in  $T^{-2}$  is dominant [18], [19], [21].

(ii)

The contact shift is given by the magnetic field generated at the nucleus by the electron magnetic moment located at the nucleus itself, in relation with the spin density at the nucleus. This effect is therefore proportional to the contact coupling constant  $A$ , according to [7], [19]  $(24)\Delta\delta_{MSC}=A\mu_B g\mu_B S(S+1)/3\gamma kT$

The observed paramagnetic shift is the sum of the DD and SC contribution:  $(25)\Delta\delta_M=\Delta\delta_{MDD}+\Delta\delta_{MSC}$

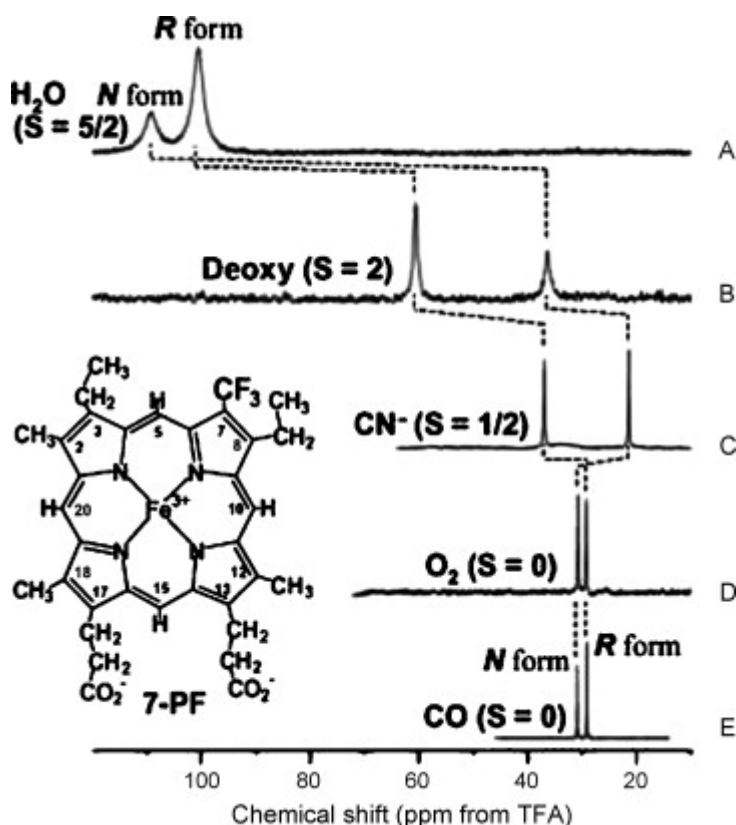
Finally, note that the theory presented here only applies to situations where the nuclear and electronic spins are located on the same molecule. When these spins are on two different species, theories of intermolecular paramagnetic relaxation enhancement and shift have to be used, the solvent being approximated either as a viscous continuum [7] or as an ensemble of discrete molecules [22], [23].

### 3. Applications to metalloproteins

The necessary requirement to obtain valuable information from  $^{19}\text{F}$  NMR signals is to introduce an exogen fluorine atom. In metalloproteins several strategies have been used and are described below.

#### 3.1. $^{19}\text{F}$ labeling heme and reconstitution of hemoproteins

This group of protein possesses unique physicochemical properties arising primarily from the presence of a heme group in the active center. Fluorinated heme syntheses associated with the reconstitution technique have been developed to introduce fluorine atom(s) into the active site of the proteins. Removal of the heme from the native protein leads to the apoprotein, which is reconstituted with a fluorinated heme. The  $^{19}\text{F}$  NMR to study hemoproteins has received an intense interest for many years [24], [25]. A recent review by Yamamoto described in detail the applicability of  $^{19}\text{F}$  NMR in b-type hemoproteins [26]. A large range of fluorine chemical shifts occur (described below; Fig. 1), corresponding to different oxidation, spin and ligation states as well as heme orientation, with respect of the protein.



1. [Download: Download full-size image](#)

Fig. 1. (A–E)  $^{19}\text{F}$  NMR spectra of various form of myoglobin substituted by the fluorinated heme 7-PF with various oxidation, spin ( $S$ ) and ligation states of heme iron at pH 7.0 and 25 °C. The two well-separated signals reflected the fractions of the two isomers (N and R forms) due to the orientation disorder. From [26] with permission.

The two well-separated signals observed in each spectrum in Fig. 1 and the unequal intensities of the signal in the spectra reflected the fractions of the two isomers due to the two possible heme orientations [27]. The pair of heme orientations differ by a 180° rotation around the 5–15 H *meso*-proton axis (Fig. 1, N and R forms).

The heme iron is either in ferrous or ferric state with a number of electrons in the 3d orbitals of 6 and 5, respectively. Depending upon the spin pairing of electrons in the 3d orbitals, ferrous heme iron can have 4, 2 or 0 unpaired electrons, corresponding to  $S = 2$ , 1 or 0, respectively and for ferric heme iron  $S = 5/2$ , 3/2 or 1/2 with 5, 3 or 1 unpaired electrons, respectively. Based on an octahedral ligand field, the energy levels of the five 3d orbitals of the iron atom are split into two groups in such a way that the energies of the  $d_{z^2}$  and  $d_{x^2-y^2}$  orbitals are higher than those of the other three orbitals  $d_{xy}$ ,  $d_{yz}$  and  $d_{xz}$ . The spin state of the hemoproteins depends on the chemical nature of the ligand. The binding of a relatively weak field strength ligand such as  $\text{H}_2\text{O}$  on ferric heme iron gives a high-spin state  $S = 5/2$  (Fig. 1A) and a low-spin state  $S = 1/2$  is achieved with a ligand such as  $\text{CN}^-$  (Fig. 1C). For the ferrous heme iron, the deoxy form (Fig. 1B) is penta-coordinated with a high-spin configuration ( $S = 2$ ) and the oxy form (Fig. 1D) or carbonmonoxy form (Fig. 1E) possesses a low-spin configuration ( $S = 0$ ). Large variations occur between the ferric derivatives of both high- and low-spin state. Also indicative of the high sensitivity of the fluorine resonances are the variations observed for the ferrous states between the paramagnetic high-spin state (Fig. 1B) and the diamagnetic states (Fig. 1D and E). Only weak differences

are observed between the diamagnetic oxyform and carbonmonoxy complexes.

Paramagnetic  $^{19}\text{F}$  NMR spectra of iron(III) porphyrins substituted with  $\text{CF}_3$  groups and *met*myoglobin reconstituted with the iron complex of a 3-trifluoromethyl porphyrin have been measured and the  $^{19}\text{F}$  shifts compared with the respective chemical shifts of the free ligands and zinc(II) complexes [25]. The shifts provided a diagnostic means for identifying the spin states.

Recently a deprotonation/protonation process in ferric myoglobin has been characterized by  $^{19}\text{F}$  NMR [28] ( $\text{pK}_a$  determination, temperature dependence of the line width, ...).

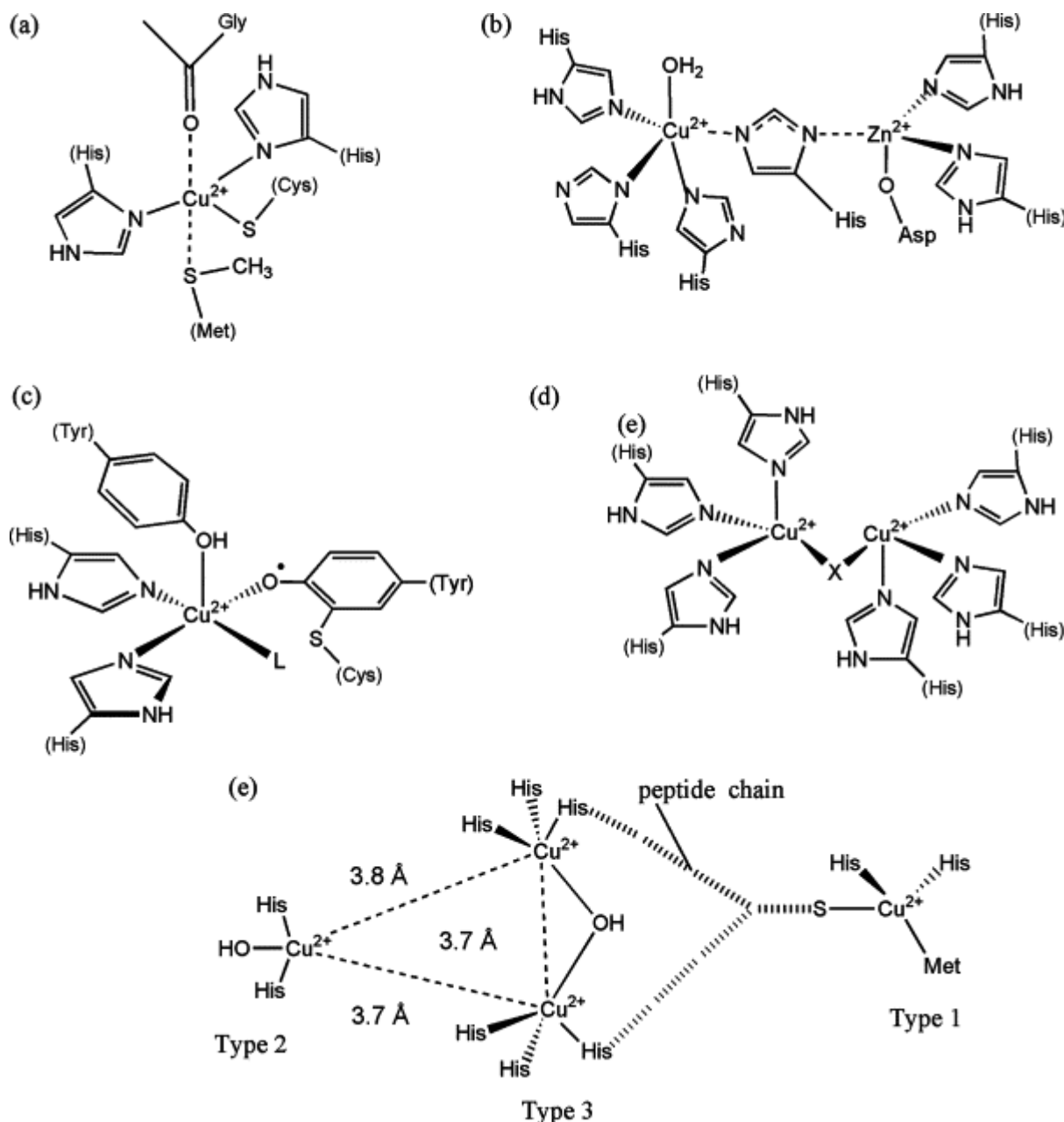
Computational methods have also been developed to predict the  $^{19}\text{F}$  NMR chemical shifts in paramagnetic metalloporphyrins [29], [30].

### 3.2. $^{19}\text{F}$ NMR and fluorinated amino acids

Synthetic methods have been developed for preparation of fluorinated derivatives of numerous common amino acids and some of them are commercially available. Introduction of fluorine on amino acid could help to distinguish between different effects. An array of molecular biology protocols (site-directed mutagenesis, incorporation of modified amino acid, ...) allows to explore the role of specific residue close to the metallic center especially from aromatic amino acids.

#### 3.2.1. Role of a targeted amino acid

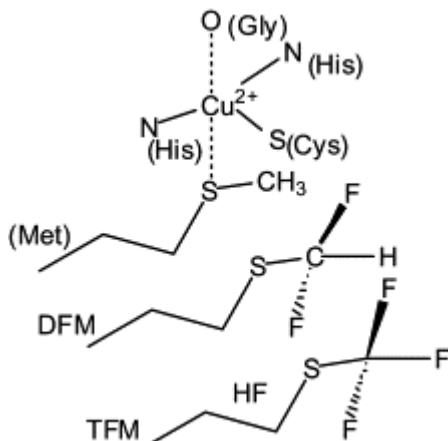
The copper proteins with the type 1 active site (or blue proteins) are involved in electron transfer and are characterized by an intense blue color in the oxidized state arising from a ligand to metal charge transfer [31]. The involvement of the axial ligand on the reduction potential has been debated for a long time [32], [33], [34]. To probe the precise role of the axial methionine in azurin (Az), a well-known type 1 copper protein (Fig. 2(a)), a series of isostructural methionine replacements have been investigated including methyl fluorinated thioethers [35]. The replacement of the methionine ligand by isostructural unnatural amino analogues was performed using the express protein ligation method [36] that couples a bacterially expressed N-terminal protein to a synthetic C-terminal peptide containing the unnatural amino acids at the axial ligand position. This approach allows to probe one variance (geometry, steric or electronic interactions, solvent exposure, ...) contrarily to multiple variances introduced by mutation.



1. [Download: Download full-size image](#)

Fig. 2. Schematic representations of active sites of copper proteins presented herein: (a) azurin (type 1), (b) superoxide dismutase (type 2), (c) galactose oxidase (type 2), (d) X = OH or OH<sub>2</sub>: catechol oxidase and tyrosinase (type 3), and (e) ascorbate oxidase (type 4 or multicopper oxidase).

As a result the correlation between reduction potentials and their axial ligand variants establishes hydrophobicity as the dominant factor in reduction potential tuning by the axial ligand. For fluorinated amino acid the fluorine atoms are both adjacent to the methionine sulfur with the difluoro and trifluoro methionine entities (DFM and TFM, respectively, see Fig. 3). In contrast to the minor changes observed in the chemical shifts on azurin containing TFM (Az-TFM), the <sup>19</sup>F chemical shift on azurin containing DFM (Az-DFM) is significantly deshielded compared to reported DFM analogue in a nonparamagnetic environment. The former interacts more strongly with the copper ions than TFM although it is somewhat less sensitive to environmental factors than DFM. Interestingly, in Az-DFM the two fluorine atoms are diastereotopic; hence their chemical shifts are nonequivalent resulting in coupling between the two fluorine as well as proton coupling to each fluorine atom. Proton-decoupled <sup>19</sup>F spectrum displays two sets of broad doublets at 85.60 and 88.15 ppm. In freely rotating DFM only a broad signal should be observed. Herein the <sup>19</sup>F chemical shift nonequivalence in Az-DFM is enhanced, indicating a restricted conformational mobility of DFM in the protein. These observations point out to what extent the <sup>19</sup>F NMR chemical shifts are environment sensitive and can get new insights on environment factors.



1. [Download: Download full-size image](#)

Fig. 3. Schematic representation of the blue copper center in Az showing replacement of the axial ligand methionine (Met) with fluorinated unnatural amino acids difluoromethionine (DFM) and trifluoromethionine (TFM). Redraw from Lu and co-workers [35].

### 3.2.2. Probe to study solvent exposure

When <sup>19</sup>F atom is solvent exposed, both chemical shift and  $T_1$  relaxation are sensitive to interaction with the solvent. The  $T_1$  relaxation time becomes longer and the <sup>19</sup>F resonance frequency shows an isotopic shift when the aqueous solvent is changed from H<sub>2</sub>O to D<sub>2</sub>O [37]. An interesting application is the use of the solvent-induced isotopic effect to estimate the degree of exposure of fluorine-containing proteins to the solvent. Illustrative example of <sup>19</sup>F NMR parameters used as a probe of solvent accessibility, is the work on a high-potential iron protein that contains a [Fe<sub>4</sub>S<sub>4</sub>] cluster from *Chromatium vinosum* [38, 39]. Fluorine-labeled protein were obtained by site-directed mutagenesis, or by inducing the expression of the protein in a medium supplemented with the fluorinated-derivative replacing a targeted amino acid (phenylalanine, tryptophan or tyrosine). <sup>19</sup>F combined with 2D <sup>1</sup>H/<sup>15</sup>N NMR experiments indicate that solvent accessibility to the cluster is similar and minimal for the native proteins, but increases significantly for mutant proteins [38]. In addition fluorine NMR provides a probe of redox-dependent conformational changes [39]. Owing to the importance of determining solvent accessibility for the understanding of substrate binding chemistry and the control of the redox properties in metalloproteins, the strategies illustrated herein are of general interest and value.

### 3.3. Fluoride ion in presence of metalloproteins

#### 3.3.1. Probe for exchangeable ligand on galactose oxidase

Galactose oxidase (GOase), a type 2 copper protein that catalyses the oxidation of primary alcohols into aldehydes [40].

Before the resolution of the X-ray structure, fluoride ion was used as a probe for the coordination site [41, 42]. The temperature and frequency dependence of the <sup>19</sup>F spin-spin  $R_2$  and spin lattice  $R_1$  relaxation rates of F<sup>-</sup> in the presence of the enzyme galactose oxidase have been analyzed. Evidence for a second coordination site for an exogenous ligand has been obtained from cyanide-fluoride competition studies, supported by <sup>19</sup>F NMR relaxation rate changes. The results are consistent with two exogenous binding sites, one equatorial with CN<sup>-</sup> and F<sup>-</sup> strongly binding the Cu<sup>II</sup> center, and one axial with F<sup>-</sup> weakly bound. These results are in accordance with X-ray crystallographic data reported later [43]. The crystal structure reveals a mononuclear center with two nitrogen from histidine, two oxygen from tyrosine (one axial and one equatorial) and an additional equatorial exogenous ligand L (L = H<sub>2</sub>O in the native enzyme). The active oxidized form possesses an equatorial bound tyrosyl radical (Fig. 2(c)).

#### 3.3.2. Binding parameters of F<sup>-</sup> to metallic centers

The interaction of fluoride anion F<sup>-</sup> with a protein can be described according to the following equilibrium characterized by  $K$  (in M<sup>-1</sup>) the stability constant. (26) E + F<sup>-</sup> ⇌ E-F<sup>-</sup>

The concentration  $C_{EF}$  of the paramagnetic complex E-F<sup>-</sup> is given by the following formula: (27)  $C_{EF} = \frac{KE_0C_{F_0}}{1 + KE_0C_{F_0}}$  where  $E_0$  is the concentration of the enzyme and  $C_{F_0}$  is the concentration of the F<sup>-</sup> anion, in large excess on  $E_0$ .

The observed relaxation rate  $R_1$  of the studied solution is the averaged mean by molar fractions for each species with the relaxation rate contributions of the anion in the bulk  $R_{10}$  and that of the anion in the complex  $R_{1M}x_{EF}$  according to the following formula: (28)  $R_1 = R_{10} + R_{1M}x_{EF}$  where  $x_{EF} = \frac{C_{EF}}{C_{F_0}}$  with  $C_{EF} \ll C_{F_0}$ , i.e.



$x_{\text{EF}}$  ■ 1.  $R_{10}$  and  $R_{1\text{M}}$  are the relaxation rates of the  $\text{F}^-$  anion in the bulk, and bonded to the paramagnetic ion center within the protein, respectively. The paramagnetic contribution to the relaxation  $R_{1\text{p}} = R_1 - R_{10}$  is therefore given using the following formula:  $(29)R_{1\text{p}} = R_{1\text{MKE01}} + KCF_0$  giving the two data, the stability constant  $K$  and the relaxation rate constant  $R_{1\text{M}}$  of the  $\text{F}^-$  bonded to the paramagnetic site of the protein. Treatments of experimental data are usually reported from the  $R_{1\text{p}}$  plot as a function of  $\log C_{\text{F0}}$  or  $T_{1\text{p}}$  as a function of  $C_{\text{F0}}$ .

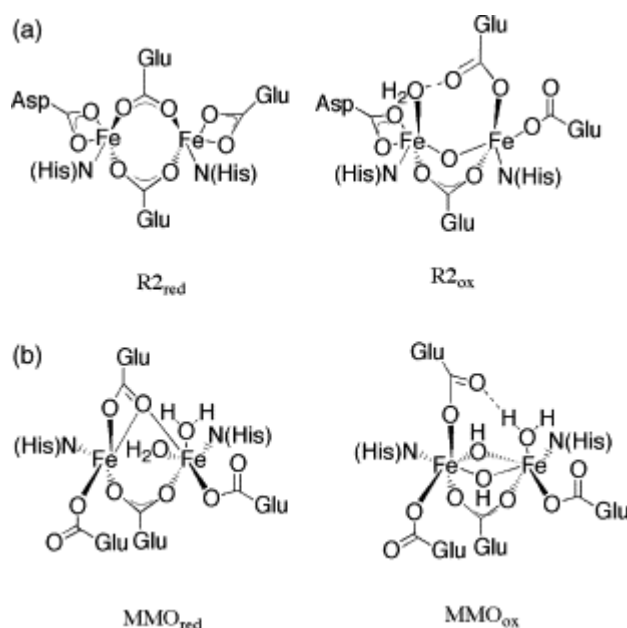
### 3.3.2.1. Binding of $\text{F}^-$ to Cu/Zn superoxide dismutase

Superoxide dismutases (SOD) are redox heterobinuclear enzymes, which protect cells against superoxide ions toxicity [44]. Copper–zinc superoxide dismutase contains in its active site an imidazolate-bridged bimetallic center, with one copper(II) and one zinc(II) ion [45] depicted in Fig. 2(b). The  $\text{Cu}^{\text{II}}$  ion is coordinated by four histidine ligands in a distorted square planar coordination sphere, and by a fifth axial water ligand. The tetrahedral zinc ion is coordinated by three histidine ligands, one of them bridging to the copper and also by a carboxylate group. Fluoride anion binds at, or near the copper sites of the bovine or yeast superoxide dismutase, and the paramagnetic metals exert an enormous effect on the fluorine  $T_1$  relaxation time in the bound state [46]. Contrarily to this large effect, the Cu/Zn SOD EPR spectra are only slightly affected by the presence of  $\text{F}^-$  up to 3 M [47]. Details of the binding have been investigated in SOD by fluoride relaxation time determinations, in concert with water-proton relaxation studies, and by examining the paramagnetically shifted resonances of ligands near the metal centers [48]. The treatment of the experimental data gives the value  $6 \text{ M}^{-1}$  for the stability constant of the anion to SOD and the value of  $1.5 \times 10^6 \text{ s}^{-1}$  for the spin-lattice relaxation rate of  $\text{F}^-$  in the  $\text{F}^-$ -SOD complex. Furthermore, the increase of the water proton relaxation rate upon addition of  $\text{F}^-$  suggest that, in this system,  $\text{F}^-$  displaces the water ligand and binds it through an hydrogen bond.

An application of this large fluorine  $T_1$  relaxation effect of such an enzyme has been used, in early stages of neuroimaging to quantify the presence of these enzymes in rat brain [49], [50].

### 3.3.2.2. $\text{F}^-$ to probe the accessibility of metallic centers in RNR and MMO

A set of experiments was done with two binuclear non-heme ferric center proteins: the small subunit of ribonucleotide reductase (RNR), protein R2 and the hydroxylase component of the soluble methane monooxygenase (MMO), protein A (Fig. 4) [51], [52]. They both catalyze oxygen activation and oxidations, but the substrates are different: for protein R2, the substrate is a specific tyrosine of the polypeptide chain in proximity to iron and for protein A, the substrates are different sized exogenous hydrocarbons, including methane. Although similarity can be found between the iron centers, there are different substrates involved, suggesting major differences between the two enzymes in terms of the accessibility of the metal ion sites. The  $\text{F}^-$  anion has been used to study the electrostatic control for the accessibility of the metal ion center. Because  $\text{Mn}^{2+}$  is a much stronger relaxing agent than  $\text{Fe}^{3+}$ , the study was carried out with the manganese-containing forms of proteins R2 and A, prepared through the iron-free apoform [53].



1. [Download: Download full-size image](#)

Fig. 4. Schematic representations of binuclear iron non-heme centers (reduced and oxidized state) in (a) R2 subunit in RNR and (b) hydroxylase component of soluble MMO.

For the Mn-A protein, treatment of the experimental data gives the value of  $3 \text{ M}^{-1}$  for the affinity constant of the anion to the protein and the value of  $0.15 \times 10^6 \text{ s}^{-1}$  for the spin-lattice relaxation rate of  $\text{F}^-$  in the  $\text{F}^-$ -Mn-A complex. For the protein Mn-R2, which contains four  $\text{Mn}^{2+}$  ions, no change of the relaxation rate of  $\text{F}^-$  has been observed at any  $\text{F}^-$  concentration. This demonstrates that the active site is buried in the protein and  $\text{F}^-$  does not gain access to the metal ion site of ribonucleotide reductase.

These results emphasize that  $^{19}\text{F}$  NMR combined to  $\text{F}^-$  binding studies is a tool to access structural and dynamics of paramagnetic metallic centers. It is a useful complement to X-ray studies to further insights into solution in assessing dynamic properties.

## 3.4. Interactions of metalloproteins with fluorinated small molecules

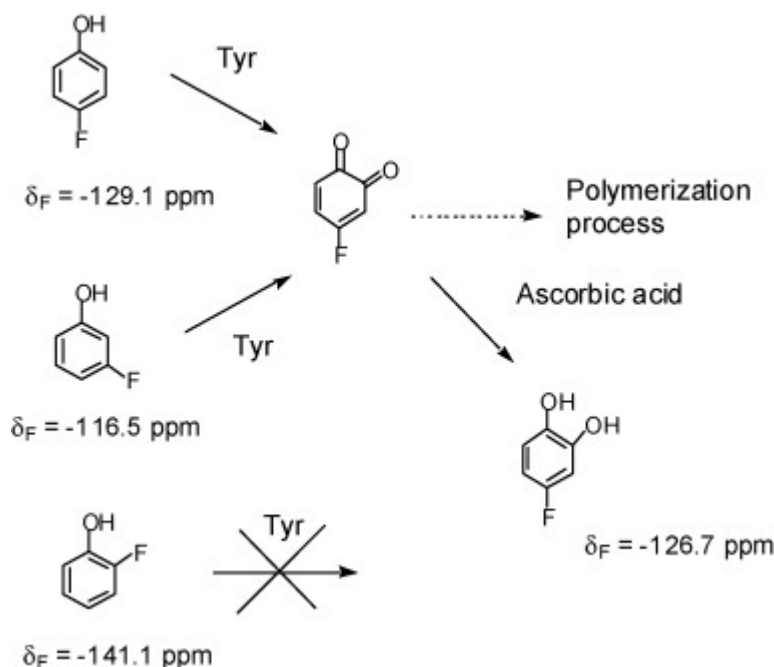
### 3.4.1. Binding and reaction of fluorophenols on tyrosinase

Tyrosinases (Tyr) and catechol oxidases (CO) are essential type 3 (two  $\text{Cu}^{2+}$  in strong interaction) dicopper-containing enzymes. Tyrosinases occur in all living organisms, whereas catechol oxidases are found in plants. Tyrosinases mediate the hydroxylation of monophenols to o-diphenols as well as the subsequent



oxidation to quinones with dioxygen, whereas catechol oxidases catalyze the two-electron oxidation of *o*-diphenols to quinones (catecholase activity) (Fig. 2(d)). In fruit and vegetables Tyr and CO are key enzymes in the browning that occurs upon bruising or long-term storage. In mammals, Tyr are responsible for skin, eye and hair pigmentation. Both enzymes possess three identified forms of the active site in the catalytic cycle: *met* ( $\text{Cu}^{\text{II}}\text{--Cu}^{\text{II}}$ ), *oxy* ( $\text{Cu}^{\text{II}}\text{--O}_2^{2-}\text{--Cu}^{\text{II}}$ ) and *deoxy* ( $\text{Cu}^{\text{I}}\text{Cu}^{\text{I}}$ ). The crystal structure of tyrosinase, has been obtained in 2006 from a recombinant enzyme [54] (the structure of *met* and *deoxy* forms of catechol oxidase were previously obtained [55]). In the *met* form all six histidine residues are conserved among Tyr and CO and exhibit a very similar binding geometry (Fig. 2(d)). The two copper(II) ions, are bridged by an aquo or an hydroxo entity.

The activity of Tyr from *Streptomyces antibioticus* toward the three isomeric fluorophenols (*o*-FP, *m*-FP, *p*-FP) was studied in detail and evidenced different behavior in solution (Fig. 5) [56]. The reaction of *m*-FP and *p*-FP in the presence of Tyr produced polymeric species. When the enzymatic reactions of *m*-FP and *p*-FP were carried out in presence of a reductant (ascorbic acid), formation of polymeric species was completely quenched. In both cases,  $^{19}\text{F}$  NMR spectra show the peak of the starting phenol and a resonance at  $-126.7$  ppm (Fig. 5) assigned to the same catechol derivative.



1. [Download: Download full-size image](#)

Fig. 5. Products formed in the early steps of the reaction of *o*-, *m*- and *p*-FP and Tyr. Fluorine chemical shifts are reported relative to  $\text{CFCl}_3$ . From Casella and co-workers [56].

Incubation of the mixture with *o*-FP shows the lack of reactivity with or without ascorbic acid: *o*-FP acts as a competitive inhibitor in the enzymatic oxidation of L-Dopa, the natural substrate of Tyr. In this work the  $^{19}\text{F}$  NMR appears as a complementary technique to the more conventional kinetic and optical spectroscopic methods. The binding studies with fluorinated phenol lead to reliable information on reaction intermediates and get new insights in mechanistic comprehension.

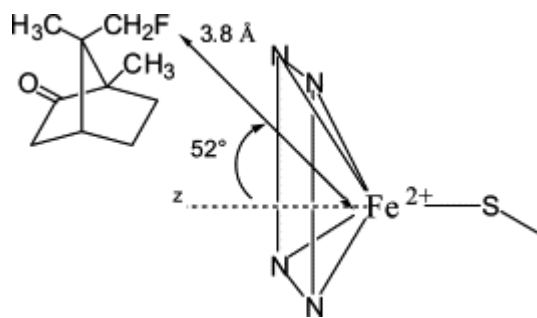
### 3.4.2. Inhibitor binding studies on ascorbate oxidase

The copper site in ascorbate oxidase (AO) is composed of four copper atoms involved in the four-electron reduction of dioxygen to water, with concomitant one-electron oxidation of the reducing organic substrate [57] (Fig. 2(e)). A type 2 and a type 3 active site together form a trinuclear cluster. An additional type 1 site is connected through a Cys-His electron transfer pathway to the trinuclear cluster at a distance of  $12 \text{ \AA}$  (Fig. 2(e)). The binding mode of the former phenolic substrates on ascorbate oxidase have been studied by Casella and co-workers [58] to provide experimental support of the location of the inhibitor binding site. Paramagnetic  $^{19}\text{F}$  NMR relaxation measurements have been performed on AO in presence of *o*-FP or *p*-FP (*m*-FP after addition on the protein causes protein precipitation). Relaxation rate  $R_{1\text{obs}}$  was measured for the fluorine atom of the inhibitor at different enzyme concentrations, in order to obtain information about the distance of fluorine from copper ions contained in the active site of AO. From the value of  $R_{1\text{obs}}$ ,  $R_{1\text{b}}$  (for the bound inhibitor when this is in fast exchange between the active site and the bulk solution) has been calculated from the equation:  $(30)R_{1\text{obs}} - R_{1\text{f}} = (R_{1\text{b}} - R_{1\text{f}})E_0K_1/I_0$  where  $R_{1\text{f}}$  is  $R_1$  for the free inhibitor,  $E_0$  and  $I_0$  are the initial enzyme and inhibitor concentrations, respectively, and  $K_1$  (unit M) is the dissociation constant for the enzyme-inhibitor complex. The paramagnetic contribution to the relaxation rate  $R_{1\text{M}}$  of the fluorine nucleus of the bound inhibitor arising from the unpaired electron on the copper center(s), is related to the copper-fluorine distance by the Solomon-Bloembergen-Morgan equation (Eqs. (8), (9), Section 2.2). As the inhibitor is not bound to the metal center, only the dipolar term has been retained in the former equation.

The  $^{19}\text{F}$  relaxation data agree with a binding site of the bound *o*- or *p*-FP inhibitors close to the type 1 copper center while the contribution to relaxation of the bound inhibitors by the type 2 Cu site is negligible (Fig. 2(e)). An estimation of the Cu-F distances for the protein complexes with *o*- and *p*-FP from the  $1/T_{1\text{b}}$  values is  $5.4$  and  $5.9 \text{ \AA}$ , respectively. Information obtained from this study is of general interest indicating that for both inhibitors and substrates of AO, the binding site is located in a pocket near the type 1 copper center.

### 3.4.3. Spatial interaction from heme and fluorinated substrate

Considering a similar approach, spatial interaction relationships between a heme and its substrate have been determined [59]. Relaxation and chemical shifts data were analyzed (in absence of strong hyperfine interactions) affording an estimation of the distance between the heme iron of ferrous cytochrome P-450 and a fluorine substrate analogue (9-fluorocamphor) (Fig. 6). Furthermore the chemical shifts data analysis gives the orientation of 9-fluorocamphor within the normal heme and the  $\text{Fe}\blacksquare\text{F}$  vector heme (Eq. (22)). The former angle and the  $\text{Fe}\blacksquare\text{F}$  distance estimated, are nearly comparable with those observed by X-ray crystallography of the ferric camphor-bound enzyme.



1. [Download: Download full-size image](#)

Fig. 6. Schematic representation of the ferrous high-spin heme iron of P-450 and 9-fluorocamphor bound in the active site based on [59].

These studies clearly demonstrate that tightly bound fluorinated substrate analogues can be successfully used to determine metal to substrate (or inhibitor) distances and geometrical information within the paramagnetic active site.

## 4. Applications to paramagnetic metal complexes of biological interest

### 4.1. Paramagnetic complexes in solution

$^{19}\text{F}$  NMR has sometimes been used with bioinspired fluorinated mimics (*vide infra*). It has also been used to study solution equilibria. A not exactly new but typical example is the study in acetone solution of the conformational equilibria in pyridine adducts of metal (cobalt, nickel) hexafluoroacetylacetonates [60]. Complexes 1:1 and 1:2 (two pyridines) were observed. In the case of the cobalt complexes, both *cis*- and *trans*-isomers were detected. At room temperature the various isomers are in rapid equilibrium and the  $^{19}\text{F}$  NMR lines are averaged. At lower temperature, the rate of exchange is slowed down, and well-resolved NMR spectra are observed for all the possible isomers. The NMR shift of the signal from the nickel complex is mainly due to the Fermi contact interaction, while the shifts of lines from the various cobalt complexes are due to both the electron–fluorine dipolar interaction, and the Fermi contact interaction.

$^{19}\text{F}$  NMR has been used to investigate intramolecular effects of copper(II) ions on the fluorine chemical shifts of dioxane complexes of copper perfluorocarboxylates [61].

In a more recent work, a  $^{19}\text{F}$  longitudinal specific relaxation rate or relaxivity ( $r_1$ ,  $\text{s}^{-1} \text{M}^{-1}$ ) study of the competition of  $\text{Gd}^{\text{III}}$  and  $\text{Lu}^{\text{III}}$  towards diethylenetriaminepentaacetate (DTPA) in water is described [62]. The  $\text{Gd}^{\text{III}}$  aqua ion and Gd-DTPA cause very different longitudinal relaxivities of the trifluoroacetate anion  $^{19}\text{F}$  nuclei. In the presence of competitor  $\text{Lu}^{\text{III}}$  ions, the relaxivity difference makes it possible to assay the concentrations of  $\text{Gd}^{\text{III}}$  aqua ions and Gd-DTPA complex from the measured paramagnetic relaxation rate enhanced by the trifluoroacetate  $^{19}\text{F}$  nuclei.

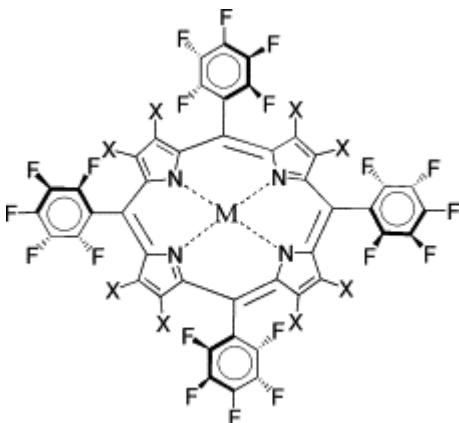
A variety of cobalt(II/III) and iron(II/III) complexes have been prepared containing the ligands 4-fluoro-2,2'-bipyridine (fbpy) and anion hexafluorophosphate [63]. Both *fac*- and *mer*-isomers of  $[\text{M}(\text{fbpy})_3]^{m+}$  have been described.  $^{19}\text{F}$  NMR chemical shifts allow the determination of the ratio of each isomer. The  $^{19}\text{F}$  chemical shifts of the ligand show minor variations with changes in the anion or solvent, while a larger variation is found as a function of the oxidation state of the metal ( $\sim 7$  ppm for the change from  $\text{Co}^{\text{III}}$  to  $\text{Co}^{\text{II}}$  and  $\sim 38$  ppm for the change from  $\text{Fe}^{\text{III}}$  to  $\text{Fe}^{\text{II}}$ ). Moreover, variable temperature  $^{19}\text{F}$  NMR allows a mechanistic study of electron transfer in  $\text{Co}^{\text{II}}(\text{bpy})_3^{2+}$ – $\text{Co}^{\text{III}}(\text{fbpy})_3^{3+}$  system.

### 4.2. Biomimetic models

#### 4.2.1. Fluorinated porphyrins

Many proteins contain a removable heme that can be easily replaced by a fluorinated fragment (see above). Taking advantages of this technique, extensive studies have been performed on synthetic porphyrins labeled by fluorine, a  $\text{CF}_3$  or a fluorinated aromatic group.

As  $^{19}\text{F}$  NMR has been extensively studied on a series of halogenated porphyrins, the former have been employed to interpret the  $^{19}\text{F}$  chemical shifts of paramagnetic compounds. A special library with different types of fluorine splitting patterns for tetrakis(pentafluorophenyl) porphyrins (TFPP) (Fig. 7) complexed with diamagnetic (Zn) and paramagnetic (Cu, Fe, Ru) metal ions [64] has been created (Table 1).



1. [Download: Download full-size image](#)

Fig. 7. Schematic representations of tetrakis(pentafluorophenyl) porphyrins (TFPP) series with  $\text{M} = \text{H}_2$ , Zn, Cu, Fe, Ru and  $\text{X} = \text{H}$ , Cl, Br. Redraw from [64].

Table 1. NMR shift for a series of fluorinated porphyrins (TFPP) from [64]

Compound	Ortho	Para	Meta
<sup>19</sup> F shifts NMR value in acetone- <i>d</i> <sub>6</sub> <sup>a</sup>			
ZnTFPP	−138.5 (d)	−154.8 (t)	−163.7 (m)
H <sub>2</sub> TFPP	−136.9 (d)	−151.7 (t)	−161.8 (m)
FeTFPP(Cl)	−105.8, −107.7	−150.2	−153.9, −156.0
FeTFPP(OH)	−108.0, −114.5	−152.0	−156.6, −158.0
(FeTFPP) <sub>2</sub> O	−133.3, −137.1	−154.8	−163.1, −164.7
CuTFPP	Not observable <sup>b</sup>		
ZnTFPPCl <sub>8</sub>	−138.9 (d)	−151.5 (t)	−163.4 (m)
H <sub>2</sub> TFPPCl <sub>8</sub>	−140.0 (d)	−149.8 (t)	−162.4 (m)
RuTFPPCl <sub>8</sub> (CO) <sup>c</sup>	−138.8, −139.3	−151.3 (t)	−163.2, −163.6
RuTFPPCl <sub>8</sub> (py) <sub>2</sub>	−136.9 (d)	−149.7 (t)	−161.1 (m)
ZnTFPPBr <sub>8</sub>	−138.4 (d)	−151.7 (t)	−163.1 (m)
H <sub>2</sub> TFPPBr <sub>8</sub>	−139.7 (d)	−150.1 (t)	−162.7 (m)
FeTFPPBr <sub>8</sub> (Cl)	−121.4, −122.3	−146.5	−158.1, −158.5
[FeTFPPBr <sub>8</sub> (Cl)] <sup>−</sup>	−124, −133	−148	−158, −160
FeTFPPBr <sub>8</sub> (py) <sub>2</sub> <sup>d</sup>	−138.6	−152.0 (t)	−163.1 (m)

a

<sup>19</sup>F NMR values are vs. CFCI<sub>3</sub> at 0 ppm. Fine structure given as follows: d, doublet of doublets; t, triplet; m, multiplet.

b

Cu(II) species are not generally observable due to their long relaxation time.

c

Major set of resonances, each with fine structure as observed in diamagnetic species; other resonances also observed, as discussed in text.

d

Values in CDCI<sub>3</sub>.

The paramagnetic shift, line broadening and fine structure of resonances from the peripheral pentafluorophenyl rings are, dependent on the symmetry and core environment of the porphyrins macrocycles, as evidenced on value collected in Table 1.

The chemical shifts of the fluorine atoms on the *meso*-phenyl rings are extremely sensitive to the metal center, to its axial ligands, and to the pyrrole carbon substituents. However, each porphyrin will have a unique spectrum. The <sup>19</sup>F NMR spectra for the unmetallated and zinc TFPP and TFPPBr<sub>8</sub> complexes (Table 1), display one set of signals each with fine structure for the *o*-, *m*-, and *p*-F.

Substitution with a paramagnetic or an axially asymmetric metal center, results in significantly different NMR spectra. High-spin, five-coordinate Fe<sup>III</sup>TFPP(Cl) and FeTFPP(OH) samples show five separate <sup>19</sup>F NMR signals that fall over a much larger window than those of the diamagnetic porphyrins. The five-coordinate (FeTFPP)<sub>2</sub>O dimer shows five peaks in its NMR spectrum (Table 1); however, the signals show significantly less broadening and appear in a much narrower window than those of the other Fe<sup>III</sup> porphyrins. Strong antiferromagnetic coupling, between the two metal centers reduces the paramagnetic shift in the <sup>19</sup>F NMR of the *p*-oxo dimer. The distinctive patterns observed in <sup>19</sup>F NMR play important roles in the structural assignment of other perhalogenated compounds. The <sup>19</sup>F NMR spectrum of Fe<sup>III</sup>TFPPBr<sub>8</sub>(Cl) shows a broadened five-signal pattern similar to that of FeTFPP(Cl). The *o*-F resonances exhibit a smaller paramagnetic shift in the perhalogenated compound. The addition of pyridine to Fe<sup>III</sup>TFPPBr<sub>8</sub>(Cl) results in reduction of the iron, and formation of the symmetric bis(pyridine) compound Fe<sup>II</sup>TFPPBr<sub>8</sub>(py)<sub>2</sub>. The identification of this compound was confirmed as low-spin iron(II) due to the sharp signals and splitting pattern consistent with an axially symmetric, diamagnetic species. Most unusual is the NMR of [Fe<sup>II</sup>TFPPBr<sub>8</sub>(Cl)]<sup>−</sup>, produced by electrochemical reduction of Fe<sup>III</sup>TFPPBr<sub>8</sub>(Cl). The relatively sharp signals support the reduction of the metal center, but the splitting of the *o*- and *m*-signals suggests an axially asymmetric porphyrin; the Fe<sup>II</sup> porphyrin appears to retain an association with the chloride ligand even in the reduced state.

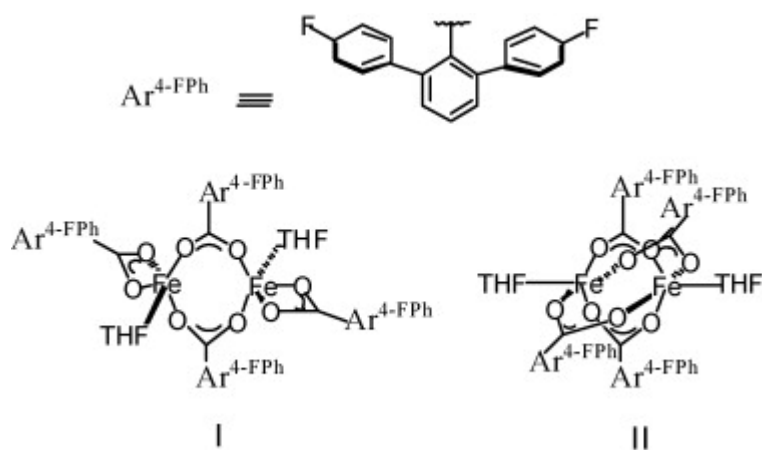
Another series with pentafluorophenyl-substituted iron(III) porphyrinates, has also been investigated and compared with the respective protonated phenyl-substituted iron porphyrinates [65]. The fluorinated phenyl compounds all show large *o*-F isotropic shifts while the *m*-F and *p*-F isotropic shifts are much smaller in magnitude, but have the same sign as the *o*-F isotropic shifts of each complex, even when there is significant spin density at the *meso*-carbons. Unlike the <sup>1</sup>H isotropic shifts, which are readily separable into dipolar and contact contributions, the <sup>19</sup>F isotropic shifts of the *o*-fluorines have an overriding large contribution from either a ligand-centered dipolar shift, or a through-space contact shift that results from direct electron cloud overlap of the *o*-fluorines with the  $\pi$  system of the porphyrin ring, but in either case, the large isotropic shift of the *o*-fluorines appears to be related to the spin density at the *meso*-carbon to which the fluorinated phenyl group is attached. Difluorovinyl deuterioporphyrin iron complexes have been synthesized and it has been shown that the <sup>19</sup>F chemical shifts were also very sensitive to the spin state of the metal and the nature of the ligand [24].

Fluorine NMR has also been used to investigate the dioxygen-reactivity of iron(II) heme [66] and heme-copper complexes [67]. Such studies provide insights on the O<sub>2</sub> binding process, on the new types of dioxygen adducts and on decomposition process.

#### 4.2.2. Fluorinated models of non-heme diiron enzymes

Carboxylate-bridged diiron centers (Fig. 4) are encountered at the active sites of enzymes that bind or activate dioxygen (hemerythrin, methane monooxygenase, ribonucleotide reductase,  $\Delta^9$ -desaturase, ...) [51], [52], and diverse synthetic models of their active sites have been synthesized and studied [68], [69]. <sup>19</sup>F NMR has been used to investigate the carboxylate coordination on diiron(II) model complexes and its shifts [70], [71]. In a very nice paper, Lippard and co-workers [72]

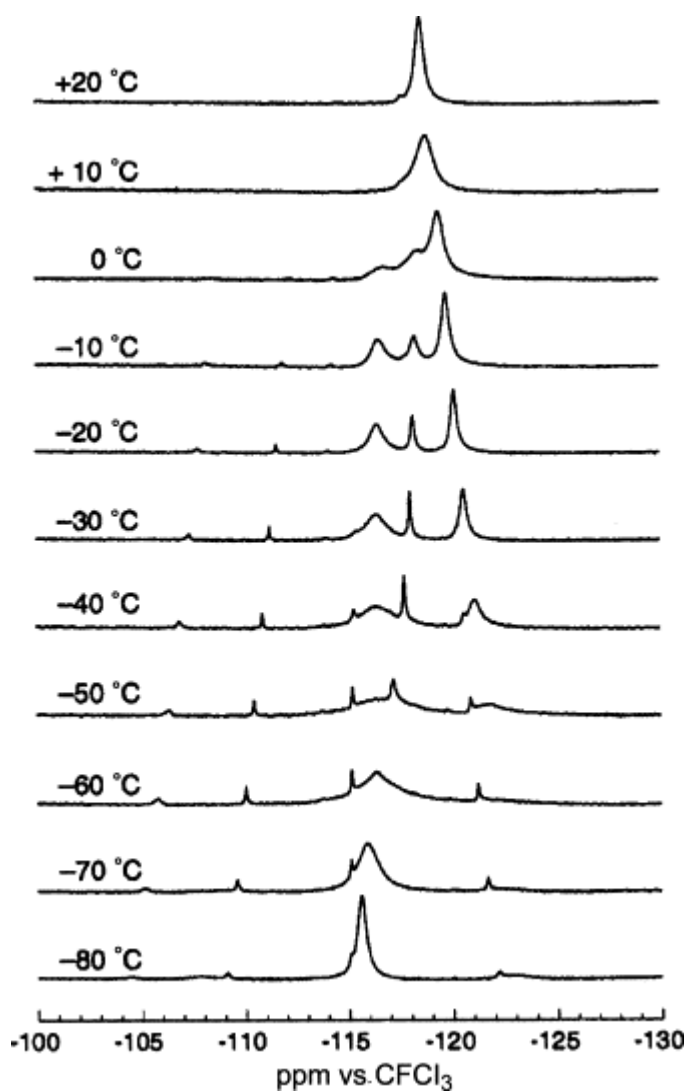
provided compelling evidence for dynamic core rearrangements via fluoro-substituted carboxylate shifts, using variable temperature  $^{19}\text{F}$  NMR from di(carboxylato) to tetra(carboxylato) diiron(II) complexes (Fig. 8).



1. [Download: Download full-size image](#)

Fig. 8. Redraw after Lippard and co-workers [72].

The dramatic spectral change of the doubly bridged diiron(II) complex I from +20 to  $-80\text{ }^{\circ}\text{C}$  (Fig. 9) is interpreted as an equilibration between doubly bridged (I) and quadruply bridged isomers (II) (Fig. 8). Temperature dependent core interconversions evidenced from  $^{19}\text{F}$  NMR, could facilitate attack by an incoming dioxygen molecule at an open coordination site for binding and activation during catalysis.



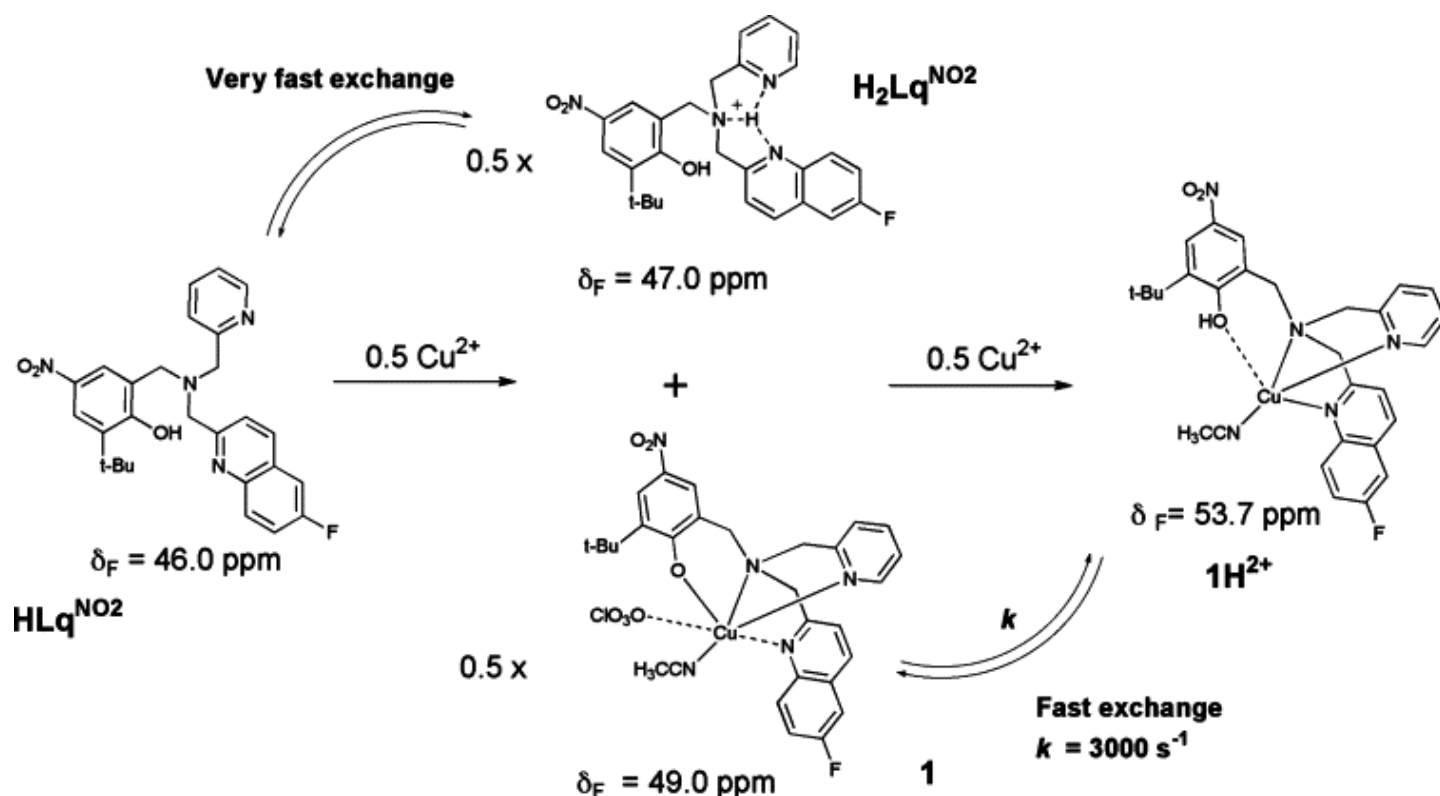
1. [Download: Download full-size image](#)

Fig. 9. Variable-temperature  $^{19}\text{F}$  NMR spectra (vs.  $\text{CFCl}_3$ ) of compound I in  $\text{CH}_2\text{Cl}_2$ . From [72] with permission.

#### 4.2.3. Fluorinated models of galactose oxidase

From copper(II) complexes of tripodal ligand  $\text{HLq}^{\text{NO}_2}$  (Fig. 10), depending on the experimental conditions (varying the respective amount of  $\text{Cu}^{2+}$ ) complexes **1** and **1H** (Fig. 10) have been isolated and characterized (X-ray) [73]. The protonation state of the phenol moiety and its position (axial vs. equatorial) were probed

by  $^{19}\text{F}$  NMR in relation with galactose oxidase enzyme (Fig. 2(c)). The fluorine NMR behavior for each species, present different chemical shifts ( $\delta_{\text{F}} = 49.0$  and  $53.7$  ppm), and different line width at half intensity of the resonance ( $\nu_{1/2} = 25$  and  $250$  Hz) for **1** and **1H**, respectively. These data clearly evidence the different environment of the copper(II) center viewed from a fluorine nucleus inserted in the ligand. In addition, from an equimolar mixture of **1** and **1H**, dynamic data were obtained through the collapse of **1** and **1H** species in chemical exchange. At the temperature of coalescence of the two signals ( $T_c = 226$  K), the rate constant of the exchange  $k = 3000 \pm 100 \text{ s}^{-1}$  is determined according to Eq. (31) [74], indicating that molecular rearrangement (proton transfer and isomerization) between **1** and **1H** is fast:  $(31)k = \pi\Delta\nu^2$



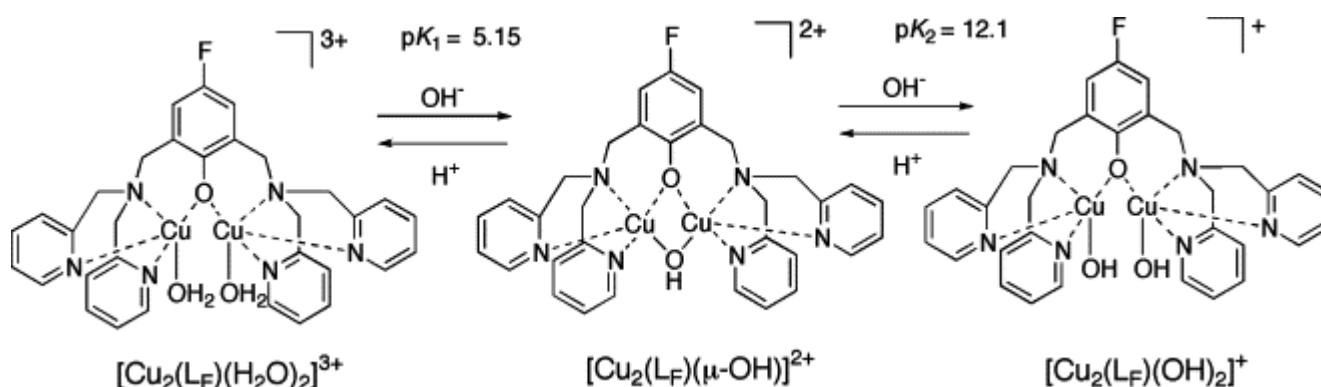
1. [Download: Download full-size image](#)

Fig. 10. Reaction of  $\text{HLq}^{\text{NO}_2}$  with  $\text{Cu}^{2+}$  (0–1 equiv. added)  $^{19}\text{F}$  NMR studies done at 282.4 MHz.

#### 4.2.4. Fluorine-labeled catechol oxidase models

##### 4.2.4.1. $^{19}\text{F}$ to monitor pH-dependent equilibrium

From ligand  $\text{HL}_\text{F}$ , a fluorinated model (Fig. 11) as been studied which is either bis aqua,  $\mu$ -hydroxo bridged or bis hydroxo according pH (the two first species have been characterized from X-ray structure determination) [75].  $^{19}\text{F}$  chemical shift are given in Table 2.



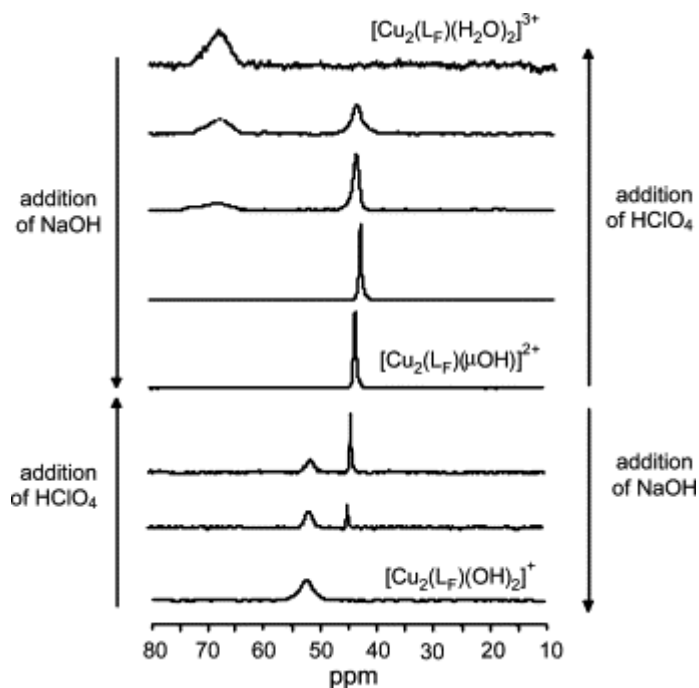
1. [Download: Download full-size image](#)

Fig. 11. pH-driven interconversions between dinuclear complexes from ligand  $\text{HL}_\text{F}$ .

Table 2.  $^{19}\text{F}$  chemical shifts (ppm vs.  $\text{C}_6\text{F}_6$ ) of  $[\text{Cu}_2(\text{L}_\text{F})(\mu\text{-OH})]^{2+}$  and  $[\text{Cu}_2(\text{L}_\text{F})(\text{H}_2\text{O})_2]^{3+}$  complexes in  $\text{D}_2\text{O}/\text{DMSO}$  (8/2, v/v)

Compound	$\delta_{\text{F}}$
$\text{HL}_\text{F}$	32.0
$[\text{Cu}^{\text{II}}_2(\text{L}_\text{F})(\text{H}_2\text{O})_2]^{3+}$	65.5
$[\text{Cu}^{\text{II}}_2(\text{L}_\text{F})(\mu\text{-OH})]^{2+}$	43.3
$[\text{Cu}^{\text{II}}_2(\text{L}_\text{F})(\text{OH})_2]^+$	51.5
$[\text{Cu}^{\text{I}}\text{Cu}^{\text{I}}(\text{L}_\text{F})(\text{OH})]^+$	22.7

The mixed valence complex  $[\text{Cu}^{\text{I}}\text{Cu}^{\text{II}}(\text{L}_\text{F})(\mu\text{OH})]^+$  has also been obtained. The  $^{19}\text{F}$  NMR spectra of the EPR silent  $\mu\text{OH}$  complex exhibits a relatively sharp peak, compared to the spectra of the bis aqua complex which presents a broad resonance peak. Despite that the fluorine atom is far from the metal centers,  $^{19}\text{F}$  chemical shifts are drastically dependent on the changes in the metal coordination spheres. Moreover,  $^{19}\text{F}$  chemical shifts are an efficient probe of the redox states of the metal centers: a  $\Delta\delta$  of 20.6 ppm is observed between the  $\mu$ -hydroxo dicopper(II) complex from  $\text{HL}_\text{F}$  and the one-electron reduced corresponding complex. The pH-driven interconversions have also been monitored by  $^{19}\text{F}$  NMR. The spectra are depicted in Fig. 12. Starting from  $[\text{Cu}_2(\text{L}_\text{F})(\mu\text{OH})]^{2+}$  spectrum, characterized by a single resonance at 43.3 ppm, addition of increasing amount of  $\text{HClO}_4$  in the solution leads to the appearance of a new signal which is clearly observed at 65.5 ppm. The new signal grows at the expense of the original resonance. In acid medium, only the new signal remains and it corresponds to the resonance found for the isolated  $[\text{Cu}_2(\text{L}_\text{F})(\text{H}_2\text{O})_2]^{3+}$  (Table 2). The same behavior can be observed, when an increasing amount of  $\text{NaOH}$  is added to the  $[\text{Cu}_2(\text{L}_\text{F})(\mu\text{OH})]^{2+}$  solution. The direct mixing of  $\text{HL}_\text{F}$ ,  $\text{Cu}(\text{ClO}_4)_2$  and  $\text{NaOH}$  leads to the same complex (putatively  $[\text{Cu}_2(\text{L}_\text{F})(\text{OH})_2]^+$ ) that the addition of  $\text{NaOH}$  to the characterized complex  $[\text{Cu}_2(\text{L}_\text{F})(\mu\text{OH})]^{2+}$ .  $^{19}\text{F}$  NMR is proved to be a powerful tool to study quantitatively the pH-dependent equilibrium between the various complexes. The equilibrium processes are slow at the  $^{19}\text{F}$  NMR time-scale, allowing the observation of the species simultaneously present in the medium. It has to be emphasized that, in the same conditions, the exchange is fast with regard to the  $^1\text{H}$  NMR time-scale in relation with small chemical shift differences between the concerned chemical species.



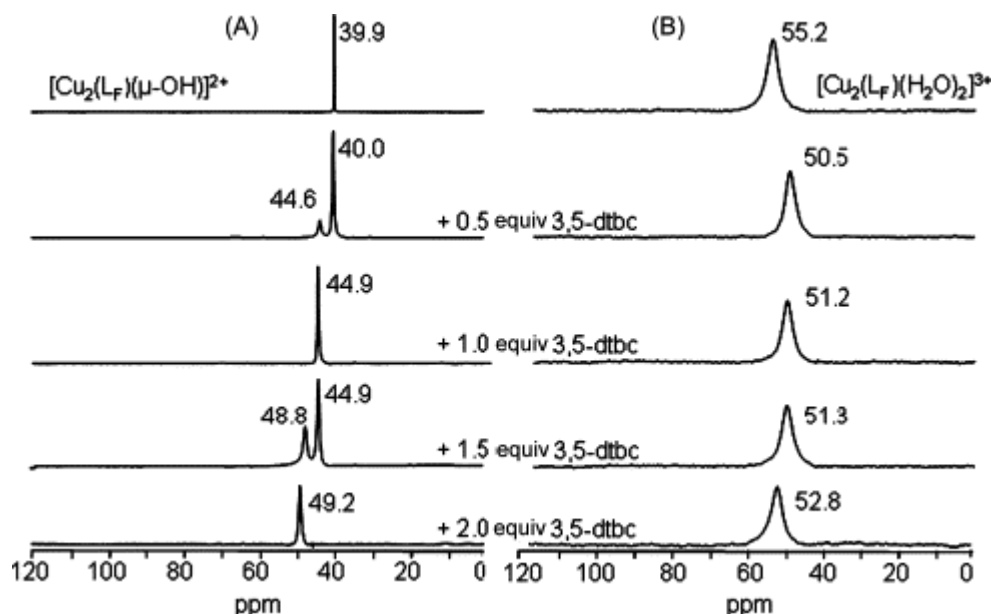
1. [Download: Download full-size image](#)

Fig. 12.  $^{19}\text{F}$  NMR monitored titration of  $[\text{Cu}_2(\text{L}_\text{F})(\text{H}_2\text{O})_2]^{3+}$  by  $\text{NaOH}$  in  $\text{D}_2\text{O}/\text{DMSO}$  (8/2, v/v). The same spectrum is obtained by addition of  $\text{HClO}_4$  to  $[\text{Cu}_2(\text{L}_\text{F})(\mu\text{OH})]^{2+}$ .  $^{19}\text{F}$  NMR spectra vs.  $\text{C}_6\text{F}_6$ .

#### 4.2.4.2. Substrate binding studies

Modifications in the coordination sphere around bridged dicopper(II) centers are easily evidenced by changes in fluorine chemical shifts on  $^{19}\text{F}$  NMR spectra. In Fig. 13 is depicted the evolution of the  $^{19}\text{F}$  NMR spectra of the  $[\text{Cu}_2(\text{L}_\text{F})(\mu\text{OH})]^{2+}$  and  $[\text{Cu}_2(\text{L}_\text{F})(\text{H}_2\text{O})_2]^{3+}$  complexes, respectively, upon progressive addition of 3,5-dtbc (3,5-di-*tert*-butylcatechol, a model substrate) in  $[D_6]\text{acetone}$  and in anaerobic conditions [76]. For  $[\text{Cu}_2(\text{L}_\text{F})(\mu\text{OH})]^{2+}$  (Fig. 13(A)), the resulting spectra exhibit well-resolved resonances. The equilibrium processes are slow compared to the  $^{19}\text{F}$  NMR time-scale, allowing the observation of a mixture of two species simultaneously present in the medium. Spectra in Fig. 13 show that two products are successively formed upon addition of substrate (one and two molar equivalents), characterized by chemical shifts at 44.9 and 49.2 ppm, respectively. The  $^{19}\text{F}$  NMR chemical shifts observed for each species are slightly modified due the presence of other compounds in solution. With the bis aqua complex  $[\text{Cu}_2(\text{L}_\text{F})(\text{H}_2\text{O})_2]^{3+}$ , a different behavior is observed (Fig. 13(B)). From the relatively broad signal of the starting material, the addition of one, then two molar equivalents of 3,5-dtbc leads to the formation of two different adducts characterized by signals located at 51.2 and 52.8 ppm, respectively. In the presence of 0.5 and 1.5 molar equivalents, the peaks broadening could also be due to exchange processes faster than the  $^{19}\text{F}$  NMR time-scale in addition to the paramagnetic properties of the isolated species.





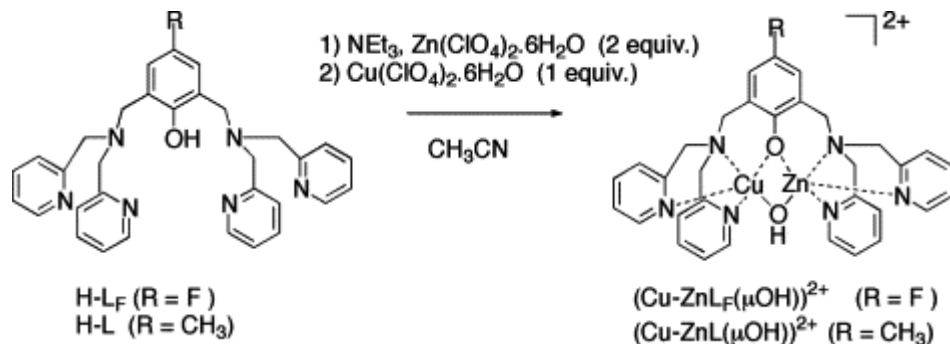
1. [Download: Download full-size image](#)

Fig. 13.  $^{19}\text{F}$  NMR (ppm vs.  $\text{C}_6\text{F}_6$ ) in  $[D_6]\text{acetone}$  for (A)  $[\text{Cu}_2(\text{L}_\text{F})(\mu\text{-OH})]^{2+}$  and (B)  $[\text{Cu}_2(\text{L}_\text{F})(\text{H}_2\text{O})_2]^{3+}$ ; upon progressive addition of 3,5-dtbc (from 0 to 2 equiv.).

These observations underline the interest of  $^{19}\text{F}$  NMR as a probe in mechanistic studies to complete UV-vis and EPR investigations. In the same conditions, the exchange is fast in regard to the  $^1\text{H}$  NMR time-scale. Both  $[\text{Cu}_2(\text{L}_\text{F})(\mu\text{-OH})]^{2+}$  and  $[\text{Cu}_2(\text{L}_\text{F})(\text{H}_2\text{O})_2]^{3+}$  species can bind one or two substrates, but *different adducts* are formed. From the hydroxo bridged species, the substrate binding occurs in two *successive* steps while on the contrary, from bis aqua complex, no successive steps can be clearly evidenced. Different binding processes of 3,5-dtbc have been evidenced herein.

#### 4.2.5. Synthesis control of heterodinuclear complexes (a $\text{Cu}^{\text{II}}\text{-Zn}^{\text{II}}$ example)

Although some non-heme proteins containing heterodinuclear metal centers are known (Fe-Zn purple acid phosphatase, Fe-Zn calcineurin, Zn-Mg in DNA polymerase I, Cu-Zn superoxide dismutase, etc.), only a limited number of synthetic models have been published, probably due to the difficulty of the syntheses. To prepare only the heterodinuclear complex from a dinucleating ligand, an experimental approach based on the ligand  $\text{HL}_\text{F}$  (Fig. 14) averred to be of particular interest to prepare the Cu-Zn complex described in Fig. 14 [77]. Furthermore, it can be directly applied in the NMR tube to test rapidly different experimental conditions to prepare the Cu-Zn complex (depicted in Fig. 14).

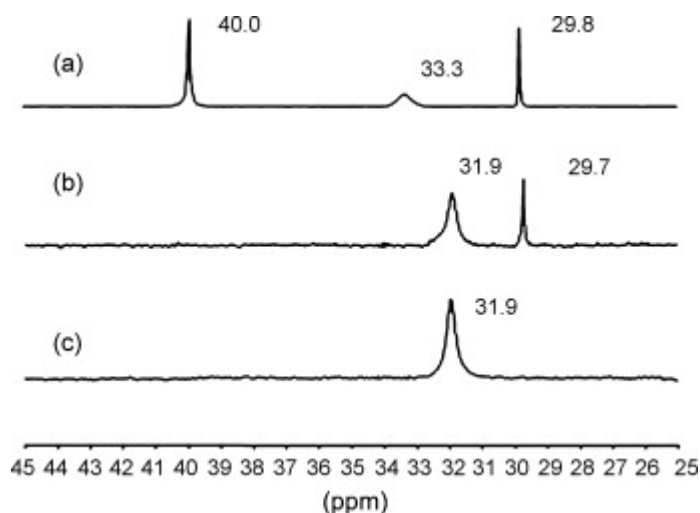


1. [Download: Download full-size image](#)

Fig. 14. Schematic preparation and structure of the  $(\mu\text{-phenoxo})(\mu\text{-hydroxo})\text{Cu}^{\text{II}}\text{-Zn}^{\text{II}}$  complexes.

Different experimental conditions were tested, upon varying the respective amount and concentration of  $\text{HL}_\text{F}$ ,  $\text{Zn}(\text{ClO}_4)_2 \cdot 6\text{H}_2\text{O}$  and  $\text{Cu}(\text{ClO}_4)_2 \cdot 6\text{H}_2\text{O}$ . Reactions are performed in acetonitrile solution with triethylamine (2 equiv.), in a NMR tube, and monitored directly by  $^{19}\text{F}$  NMR. In Fig. 15 are depicted the spectra corresponding to the more significant experimental pathways. Mixing  $\text{HL}_\text{F}$ ,  $\text{Zn}(\text{ClO}_4)_2 \cdot 6\text{H}_2\text{O}$  with  $\text{Cu}(\text{ClO}_4)_2 \cdot 6\text{H}_2\text{O}$  at 1:1:1 ratio (statistical method) leads to a mixture of different complexes.  $^{19}\text{F}$  NMR spectroscopy exhibits three well-resolved resonances (Fig. 15(a)). Comparison with the  $\delta_\text{F}$  of the homodinuclear  $(\mu\text{-phenoxo})(\mu\text{-hydroxo})$   $(\text{Cu}^{\text{II}}\text{-Cu}^{\text{II}}$  or  $\text{Zn}^{\text{II}}\text{-Zn}^{\text{II}})$  complexes isolated after an independent preparation, allowed the unambiguous identification of the bis copper (40.0 ppm) and the bis zinc (29.7 ppm) resonances, despite the small deviation of  $^{19}\text{F}$  NMR chemical shift observed between these isolated complexes (40.7 and 30.4 ppm, respectively) and those in the reaction mixture. When using an excess of the zinc salt ( $\text{HL}_\text{F}$ ,  $\text{Zn}(\text{ClO}_4)_2 \cdot 6\text{H}_2\text{O}$ ,  $\text{Cu}(\text{ClO}_4)_2 \cdot 6\text{H}_2\text{O}$  at 1:2:1 ratio) the dicopper complex is not observed, but still leads to a mixture (Fig. 15(b)). Interestingly, by using this last procedure, in a 2-fold diluted medium, and a later addition of the copper salt, only the compound with the signal at 31.9 ppm is obtained (Fig. 15(c)) and it can easily be isolated and characterized as the  $[\text{Cu-ZnL}_\text{F}(\mu\text{OH})](\text{ClO}_4)_2$ . The  $^{19}\text{F}$  NMR spectrum of this copper-zinc complex exhibits a relatively broad resonance compared to the spectra of the diamagnetic bis zinc complex and to the paramagnetic bis copper(II) complex (with no EPR observed spectrum), indicating a strong antiferromagnetic interaction between the two copper atoms as in the dimeric dinuclear copper(II) complex from  $\text{HL}$  [78]. EPR data for the heterodinuclear complex reveals the usual features of a mononuclear copper(II) complex with axial symmetry. These observations, taken together, indicate that the observed  $^{19}\text{F}$  signals are very sensitive to the local environment (structural and magnetic) of this dimetallic center.





1. [Download](#): [Download full-size image](#)

Fig. 15.  $^{19}\text{F}$  NMR for (a)  $\text{HL}_\text{F} + 2\text{Et}_3\text{N} + 1\text{Zn}(\text{ClO}_4)_2 \cdot 6\text{H}_2\text{O} + 1\text{Cu}(\text{ClO}_4)_2 \cdot 6\text{H}_2\text{O}$  ( $10^{-3}$  M in  $\text{CD}_3\text{CN}$ ); (b)  $\text{HL}_\text{F} + 2\text{Et}_3\text{N} + 2\text{Zn}(\text{ClO}_4)_2 \cdot 6\text{H}_2\text{O} + 1\text{Cu}(\text{ClO}_4)_2 \cdot 6\text{H}_2\text{O}$  ( $10^{-3}$  M in  $\text{CD}_3\text{CN}$ ); (c)  $\text{HL}_\text{F} + 2\text{Et}_3\text{N} + 2\text{Zn}(\text{ClO}_4)_2 \cdot 6\text{H}_2\text{O} + 1\text{Cu}(\text{ClO}_4)_2 \cdot 6\text{H}_2\text{O}$  ( $10^{-5}$  M in  $\text{CD}_3\text{CN}$ ).  $^{19}\text{F}$  NMR spectra vs.  $\text{C}_6\text{F}_6$ .

Then, the same experimental procedure was applied with HL and enabled us to prepare and isolate easily the corresponding heterodinuclear  $[\text{Cu}-\text{ZnL}(\mu\text{OH})](\text{ClO}_4)_2$  complex, in good yield.

The current statistic process used to prepare heterobinuclear complexes leads to mixtures of homo and heterobinuclear species and no rapid method is available to analyze these mixtures before separation of the complexes.  $^{19}\text{F}$  NMR can be a viable tool for adjusting experimental procedure in order to prepare, under control and good yield, heterodinuclear complexes.

## 5. Conclusion

Some conclusions emerge from these successful investigations of paramagnetic centers presented in this review.

The problem of spectral overlap encountered in  $^1\text{H}$  NMR is removed in  $^{19}\text{F}$  NMR. Simplification on the spectra, the easiness of (bio)synthetic incorporation and the low-perturbing nature of fluorine substitution (in size and electronic density especially at aromatic positions) emphasizes the benefit of this approach.  $^{19}\text{F}$  chemical shifts as well as relaxation times lead to complementary and accurate information. The examples given in this review show that  $^{19}\text{F}$  NMR can be efficiently used to study: (i) exchange equilibria according pH between different species, (ii) equilibria between stereoisomers, (iii) binding and spatial interactions of substrates to paramagnetic metal centers, (iv) redox and spin states of the metallic centers, (v) solvent exposure of active metallic center, and (vi) evidence of reaction intermediates.

Despite this, it is surprisingly underused.  $^{19}\text{F}$  NMR is proved to be a powerful tool for structural as well as mechanistic (catalytic) studies for paramagnetic metal complexes and metalloenzymes.

## Acknowledgement

The authors thank Dr. Pascal H. Fries (CEA, Grenoble) for fruitful discussions and for careful reading of this manuscript.

## References

[1]

J.T. Gerig

Methods Enzymol., 117 (1989), p. 3

[View PDFView article](#)

[2]

J.T. Gerig

Prog. Nucl. Magn. Reson., 26 (1994), p. 293

and references herein

[View PDFView articleView in Scopus](#)

[3]

B.D. Sykes, W.E. Hull

Methods Enzymol., 49 (1978), p. 270

[View PDFView articleView in Scopus](#)

[4]

Presentation of NMR data for publication in Chemical Journals: B—conventions relating to spectra from nuclei other than protons, Pure Appl. Chem., 1976, p. 217.

[Google Scholar](#)

[5]

G.N. La Mar, W.D. Horrocks, R.H. Holm (Eds.), NMR of Paramagnetic Molecules: Principles and Applications, Academic Press, New York (1973)

[\[6\]](#)

I. Bertini, C. Luchinat

Coord. Chem. Rev., 150 (Special issue) (1996), p. 1

[View in Scopus](#)

[\[7\]](#)

I. Bertini, C. Luchinat, G. Parigi (Eds.), Solution NMR of Paramagnetic Molecules, Elsevier, Amsterdam (2001)

[\[8\]](#)

I. Solomon

Phys. Rev., 99 (1955), p. 559

[View in Scopus](#)

[\[9\]](#)

I. Solomon, N. Bloembergen

J. Chem. Phys., 25 (1956), p. 261

[View at publisherCrossref](#)

[\[10\]](#)

R.E. Connick, D. Fiat

J. Chem. Phys., 44 (1966), p. 4103

[View at publisherCrossrefView in Scopus](#)

[\[11\]](#)

J. Reuben, G.H. Reed, M. Cohn

J. Chem. Phys., 52 (1970), p. 1617

[View in Scopus](#)

[\[12\]](#)

N. Benetis, J. Kowalewski, L. Nordenskiöld, H. Wennerström, P.O. Westlund

Mol. Phys., 48 (1983), p. 329

[View at publisherCrossrefView in Scopus](#)

[\[13\]](#)

J. Kowalewski

D.M. Grant, R.K. Harris (Eds.), Encyclopedia of Nuclear Magnetic Resonance, vol. T5, J. Wiley (1996), p. 3456

[\[14\]](#)

P.H. Fries

Mol. Phys., 48 (1983), p. 503

[View at publisherCrossrefView in Scopus](#)

[\[15\]](#)

E. Belorizky, P.H. Fries, L. Helm, J. Kowalewski, D. Kruk, R.R. Sharp, P.O. Westlund

J. Chem. Phys. (2008), p. 052315

[View in Scopus](#)

[\[16\]](#)

P.H. Fries, E. Belorizky

J. Chem. Phys., 126 (2007), p. 204503

[View in Scopus](#)

[\[17\]](#)

D. Canet, J.C. Boubel, E. Canet-Soulas

Wiley (Ed.), Nuclear Magnetic Resonance: Concepts and Methods, Chichester, New York (1996)

[Google Scholar](#)

[\[18\]](#)

B. Bleaney

J. Magn. Res., 8 (1972), p. 91

[View PDFView articleView in Scopus](#)

[\[19\]](#)

J.A. Peters, J. Huskens, D.J. Raber

Prog. Nucl. Magn. Reson., 28 (1996), p. 283

[View PDFView articleView in Scopus](#)

[\[20\]](#)

G.N. La Mar, G.R. Eaton, R.H. Holm, F.A. Walker

J. Am. Chem. Soc., 95 (1973), p. 63

[View at publisher](#)

[CrossrefView in Scopus](#)

[\[21\]](#)

L. Di Bari, P. Salvadori

Coord. Chem. Rev., 249 (2005), p. 2854

[View PDF](#)[View article](#)[View in Scopus](#)

[\[22\]](#)

P. Fries, G.N. Patey

J. Chem. Phys., 80 (1984), p. 6253

[\[23\]](#)

M. Jeannin, E. Belorizky, P. Fries, W. Gorecki

J. Phys. II, 3 (1993), p. 1511

[\[24\]](#)

C. Poliard, J.-F. Briand, F. Tortevoie, J. Leroy, G. Simonneaux, A. Bondon

Magn. Reson. Chem., 39 (2001), p. 615

[View in Scopus](#)

[\[25\]](#)

H. Toi, M. Homma, A. Suzuki, H. Ogoshi

J. Chem. Soc., Chem. Commun. (1985), p. 1791

[View in Scopus](#)

[\[26\]](#)

A. Yamamoto

Annu. Rep. NMR Spectrosc., 57 (2006), p. 52

and references herein

[\[27\]](#)

G.N. La Mar, D.L. Budd, D.B. Viscio, K.M. Smith, K.C. Langry

Proc. Natl. Acad. Sci. U.S.A., 75 (1978), p. 5755

[View at publisher](#)[Crossref](#)[View in Scopus](#)

[\[28\]](#)

S. Nagao, Y. Hirai, A. Suzuki, A. Yamamoto

J. Am. Chem. Soc., 127 (2005), p. 4146

[View at publisher](#)

[Crossref](#)[View in Scopus](#)

[\[29\]](#)

J.G. Pearson, B. Montez, H. Le, E. Oldfield, E.Y.T. Chien, S.G. Sligar

Biochemistry, 36 (1997), p. 3590

[View in Scopus](#)

[\[30\]](#)

J. Mao, Y. Zhang, E. Oldfield

J. Am. Chem. Soc., 124 (2002), p. 13911

[View in Scopus](#)

[\[31\]](#)

E.I. Solomon, M.J. Baldwin, M.D. Lowery

Chem. Rev., 92 (1992), p. 521

[View at publisher](#)

[Crossref](#)[View in Scopus](#)

[\[32\]](#)

B.G. Malmström, P. Wittung-Stafshede

Coord. Chem. Rev., 185–186 (1999), p. 127

[View PDF](#)[View article](#)[View in Scopus](#)

[\[33\]](#)

H.B. Gray, B.G. Malmström, R.J.P. Williams

J. Biol. Inorg. Chem., 5 (2000), p. 551

[View in Scopus](#)

[\[34\]](#)

E.I. Solomon, R.K. Szilagy, S. DeBeer George, L. Basumallick

Chem. Rev., 104 (2004), p. 419

[View in Scopus](#)

[\[35\]](#)

D.K. Garner, M.D. Vaughan, H.J. Hwang, M.G. Savelieff, S.M. Berry, J.F. Honek, Y. Lu

J. Am. Chem. Soc., 128 (2006), p. 15608

[View at publisher](#)

[CrossrefView in Scopus](#)

[36]

K. Severinov, T.W. Muir

J. Biol. Chem., 273 (1998), p. 16205

[View PDFView articleView in Scopus](#)

[37]

P.E. Hansen, H.D. Dettman, B.D. Sykes

J. Magn. Res., 62 (1985), p. 487

[View PDFView articleView in Scopus](#)

[38]

D. Li, A. Agarwal, J.A. Cowan

Inorg. Chem., 35 (1996), p. 1121

[View in Scopus](#)

[39]

D. Li, A. Soriano, J.A. Cowan

Inorg. Chem., 35 (1996), p. 1980

[View in Scopus](#)

[40]

J.W. Whittaker

A.S.H. Sigel (Ed.), Metal Ions in Biological Systems, Marcel Dekker, New York (1994), p. 315

[Google Scholar](#)

[41]

R.J. Kurland, B.J. Marwedel

J. Phys. Chem., 83 (1979), p. 1422

[View at publisher](#)

[CrossrefView in Scopus](#)

[42]

B.J. Marwedel, D.J. Kosman, R.D. Bereman, R.J. Kurland

J. Am. Chem. Soc., 103 (1981), p. 2842

[View at publisher](#)

[CrossrefView in Scopus](#)

[43]

N. Ito, N.E.V. Phillips, K.D.S. Yadav, P.F. Knowles

J. Mol. Biol., 238 (1994), p. 794

[View PDFView article](#)

[44]

I. Fridovich

Annu. Rev. Biochem., 11 (1975), p. 147

[View at publisherCrossrefView in Scopus](#)

[45]

J.A. Tainer, E.D. Getzoff, J.S. Richardson, D.C. Richardson

Nature, 306 (1983), p. 284

[View at publisher](#)

[CrossrefView in Scopus](#)

[46]

P. Viglino, A. Rigo, R. Stevanato, G.A. Ranieri, G. Rotilio, L. Calabrese

J. Magn. Res., 34 (1979), p. 265

[View PDFView articleView in Scopus](#)

[47]

I. Bertini, E. Borghi, C. Luchinat, A. Scozzafava

J. Am. Chem. Soc., 103 (1981), p. 7779

[View at publisher](#)

[CrossrefView in Scopus](#)

[48]

L. Banci, I. Bertini, C. Luchinat, A. Scozzafava, P. Turano

Inorg. Chem., 28 (1989), p. 2377

[View at publisher](#)

[Crossref](#)

[\[49\]](#)

M. Scarpa, P. Viglino, F. Momo, F. Bracco, L. Battistin, A. Rigo  
J. Biochem. Biophys. Methods, 22 (1991), p. 135

[View PDF](#)[View article](#)[View in Scopus](#)

[\[50\]](#)

M. Scarpa, F. Vianello, A. Rigo, P. Viglino, F. Bracco, L. Battistin  
Magn. Reson. Chem., 11 (1994), p. 697

[\[51\]](#)

A.L. Feig, S.J. Lippard  
Chem. Rev., 94 (1994), p. 759

[View at publisher](#)

[Crossref](#)[View in Scopus](#)

[\[52\]](#)

L.J. Que, Y. Dong  
Acc. Chem. Res., 29 (1996), p. 190

[View in Scopus](#)

[\[53\]](#)

S. Hamman, M. Atta, A. Ehrenberg, P. Wilkins, H. Dalton, C. Béguin, M. Fontecave  
Biochem. Biophys. Res. Commun., 195 (1993), p. 594

[View PDF](#)[View article](#)[View in Scopus](#)

[\[54\]](#)

Y. Matoba, T. Kumagai, A. Yamamoto, H. Yoshitsu, M. Sugiyama  
J. Biol. Chem., 281 (2006), p. 8981

[View PDF](#)[View article](#)[View in Scopus](#)

[\[55\]](#)

T. Klabunde, C. Eicken, J.C. Sacchettini, B. Krebs  
Nat. Struct. Biol., 5 (1998), p. 1084

[View in Scopus](#)

[\[56\]](#)

G. Battaini, E. Monzani, L. Casella, E. Lonardi, A.W.J.W. Tepper, G.W. Canters, L. Bubacco  
J. Biol. Chem., 277 (2002), p. 44606

[View PDF](#)[View article](#)[View in Scopus](#)

[\[57\]](#)

A. Messerschmidt  
K.D. Karlin, Z. Tyeklar (Eds.), Bioinorganic Chemistry of Copper, Chapman & Hall, New York (1993), p. 471

[View at publisher](#)

[Crossref](#)[Google Scholar](#)

[\[58\]](#)

L. Santagostini, M. Gullotti, L. De Gioia, P. Fantucci, E. Franzini, A. Marchesini, E. Monzani, L. Casella  
Int. J. Biochem. Cell Biol., 36 (2004), p. 881

[View PDF](#)[View article](#)[View in Scopus](#)

[\[59\]](#)

G.B. Crull, J.W. Kennington, A.R. Garber, P.D. Ellis, J.H. Dawson  
J. Biol. Chem., 264 (1989), p. 2649

[View PDF](#)[View article](#)[View in Scopus](#)

[\[60\]](#)

P.F. Richardson, R.W. Kreilick  
Inorg. Chem., 20 (1981), p. 1978

[View at publisher](#)

[Crossref](#)[View in Scopus](#)

[\[61\]](#)

A.V. Sobolev, S.A. Krupoder, T.I. Liskovskaya, V.S. Danilovich  
J. Struct. Chem., 41 (2000), p. 338

[View in Scopus](#)

[\[62\]](#)

C.S. Bonnet, P. Fries  
Magn. Reson. Chem., 41 (2003), p. 782

[View at publisher](#)

[Crossref](#)[View in Scopus](#)

[\[63\]](#)

F. Qu, T.Q. Nguyen, A.F. Janzen  
J. Fluorine Chem., 94 (1999), p. 15

[View PDF](#)[View article](#)[View in Scopus](#)

[\[64\]](#)

E.R. Birnbaum, J.A. Hodge, M.W. Grinstaff, W.P. Shaefer, L. Henling, J.A. Labinger, J.E. Bercaw, H.B. Gray  
Inorg. Chem., 34 (1995), p. 3625

[View at publisher](#)

[Crossref](#)[View in Scopus](#)

[\[65\]](#)

L. Yatsunyk, F.A. Walker  
Inorg. Chim. Acta, 337 (2002), p. 266

[View PDF](#)[View article](#)[View in Scopus](#)

[\[66\]](#)

R.A. Ghiladi, R.M. Kretzer, I. Guzei, A.L. Rheingold, Y.-M. Neuhold, K.R. Hatwell, A.D. Zuberbühler, K.D. Karlin  
Inorg. Chem., 40 (2001), p. 5754

[View in Scopus](#)

[\[67\]](#)

R.A. Ghiladi, E.E. Chufan, D. del Rio, E.I. Solomon, C. Krebs, B.H. Huynh, H.-W. Huang, P. Moënne-Loccoz, S. Kaderli, M. Honecker, A.D. Zuberbühler, L. Marzilli, R.J. Cotter, K.D. Karlin  
Inorg. Chem., 46 (2007), p. 3889

[Crossref](#)[View in Scopus](#)

[\[68\]](#)

J. Du Bois, T.J. Mizoguchi, S.J. Lippard  
Coord. Chem. Rev., 200–202 (2000), p. 443

[View PDF](#)[View article](#)[View in Scopus](#)

[\[69\]](#)

E.V. Tshuva, S.J. Lippard  
Chem. Rev., 104 (2004), p. 987

[View in Scopus](#)

[\[70\]](#)

K.S. Hagen, R. Lachicotte, A. Kitaygorodskiy  
J. Am. Chem. Soc., 115 (1993), p. 12617

[Crossref](#)[View in Scopus](#)

[\[71\]](#)

R. Lachicotte, A. Kitaygorodskiy, K.S. Hagen  
J. Am. Chem. Soc., 115 (1993), p. 8883

[Crossref](#)[View in Scopus](#)

[\[72\]](#)

D. Lee, S.J. Lippard  
Inorg. Chem., 41 (2002), p. 2704

[View in Scopus](#)

[\[73\]](#)

F. Michel, S. Hamman, F. Thomas, C. Philouze, I. Gautier-Luneau, J.L. Pierre  
Chem. Commun. (2006), p. 4122

[Crossref](#)[View in Scopus](#)

[\[74\]](#)

J.A. Pople, W.G. Schneider, H.J. Bernstein  
High-Resolution Nuclear Magnetic Resonance  
McGraw-Hill, New York (1959)  
p. 223

[Google Scholar](#)

[\[75\]](#)

C. Belle, C. Béguin, I. Gautier-Luneau, S. Hamman, C. Philouze, J.L. Pierre, F. Thomas, S. Torelli, E. Saint Aman, M. Bonin  
Inorg. Chem., 41 (2002), p. 479

[View in Scopus](#)

[\[76\]](#)

S. Torelli, C. Belle, S. Hamman, J.L. Pierre, E. Saint Aman  
Inorg. Chem., 41 (2002), p. 3983

[View in Scopus](#)

[77]

S. Torelli, C. Belle, I. Gautier-Luneau, S. Hamman, J.L. Pierre

Inorg. Chim. Acta, 333 (2002), p. 144

[View PDF](#)[View article](#)[View in Scopus](#)

[78]

S. Torelli, C. Belle, I. Gautier-Luneau, J.L. Pierre, E. Saint Aman, J.M. Latour, L. Le Pape, D. Luneau

Inorg. Chem., 39 (2000), p. 3526

[View in Scopus](#)

## Cited by (18)

### [Charge density distribution effect in pyrrolidine-fused chlorins on microbial uptake and antimicrobial photoinactivation of microbial pathogens](#)

2021, Journal of Photochemistry and Photobiology B: Biology

Citation Excerpt :

This structural feature produces an increment of the amphiphilic character, which can be advantageous for the uptake of microbial cells. Moreover, PFP groups can also be used for  $^{19}\text{F}$  magnetic resonance imaging in combination with red fluorescence imaging of the chlorin macrocycle for biomedical investigations [40–42]. In addition, fluorinated porphyrinoids usually have higher photostability towards oxidative degradation than the corresponding unsubstituted fluorine analogs [15].

Show abstract

### [New frontiers and developing applications in \$^{19}\text{F}\$ NMR](#)

2013, Progress in Nuclear Magnetic Resonance Spectroscopy

Citation Excerpt :

Indeed, this has been used to identify cellular compartmentation based on the ability of the contrast agent to relax extracellular, but not intracellular material [159]. Direct relaxation can also be achieved by including F or  $\text{CF}_3$  in a paramagnetic ligand complex [113,160]. If  $^{19}\text{F}$  is attached very close to a paramagnetic center, such as  $\text{Gd}^{3+}$  or  $\text{Fe}^{3+}$ , the local paramagnetic relaxation effect (PRE) can strongly influence the fluorine atom.

### [Fluorinated porphyrinoids and their biomedical applications](#)

2011, Journal of Photochemistry and Photobiology C: Photochemistry Reviews

Citation Excerpt :

Thus,  $^{19}\text{F}$  NMR detects the fluorine containing molecule selectively and reduces the problem with background signals. Moreover, this technique is more sensitive for changes in the microenvironment than  $^1\text{H}$  NMR due to larger chemical shifts [34–36].  $^{19}\text{F}$  NMR can be used for in vitro investigation of molecules containing fluorine, e.g. their interaction mechanisms with receptors, anticancer drug localization in tumors and normal tissues.

Show abstract

### [New porphyrins tailored as biodiesel fluorescent markers](#)

2011, Dyes and Pigments

Citation Excerpt :

The resulting equations extracted from the curves were used to quantify markers 2 and 3 in the biodiesel samples. The synthesis of the novel tetra-functionalized (pentafluorophenyl)porphyrins 2 and 3 was accomplished by means of the highly selective nucleophilic substitution of the four para-fluoro atoms in the 5,10,15,20-meso-tetrakis-(pentafluorophenyl)porphyrin (1) using an improvement to a described procedure [17]. The products were obtained in high yields (98 and 95%, respectively) by using hexadecan-1-ol, in THF, or ethanol as nucleophiles under reflux, as shown in Scheme 1.

Show abstract

### [NMR spectroscopic investigations of transition metal complexes in organometallic and bioinorganic chemistry](#)

2024, Bulletin of the Korean Chemical Society

### [Applications of Fluorous Porphyrinoids: An Update<sup>†</sup>](#)

2021, Photochemistry and Photobiology

[View all citing articles on Scopus](#)

[View Abstract](#)

Copyright © 2008 Elsevier B.V. All rights reserved.



## Recommended articles

### [Accurate fragment-based 51-V chemical shift predictions in molecular crystals](#)

Solid State Nuclear Magnetic Resonance, Volume 114, 2021, Article 101733

Amanda Mathews, Joshua D. Hartman

[View PDF](#)

### [Refining the anchor: Optimizing the performance of cyclometallated ruthenium\(II\) dyes in p-type dye sensitized solar cells](#)

Polyhedron, Volume 140, 2018, pp. 122-128

Nathalie Marinakis, ..., Catherine E. Housecroft

[View PDF](#)

### [Long-lived negative molecular ions of TCNQ formed by the resonant capture of electrons with above zero energies](#)

Chemical Physics Letters, Volume 711, 2018, pp. 81-86

Olga G. Khvostenko, ..., Svetlana N. Tseplina

[View PDF](#)

Show 3 more articles

## Article Metrics

### Citations

- Citation Indexes: 18

### Captures

- Readers: 42



[View details](#)

- [About ScienceDirect](#)
- [Remote access](#)
- [Shopping cart](#)
- [Advertise](#)
- [Contact and support](#)
- [Terms and conditions](#)
- [Privacy policy](#)

Cookies are used by this site. [Cookie settings](#) | [Your Privacy Choices](#)

All content on this site: Copyright © 2024 Elsevier B.V., its licensors, and contributors. All rights are reserved, including those for text and data mining, AI training, and similar technologies. For all open access content, the Creative Commons licensing terms apply.